Controls on Subtropical Cloud Reflectivity during a Waterbelt Scenario for the Cryogenian Glaciations

Christoph Braun,[a] Aiko Voigt,[b] Corinna Hoose,[a] Annica M. L. Ekman,[c] and Joaquim G. Pinto[a]

[a] *Institute of Meteorology and Climate Research, Karlsruhe Institute of Technology, Karlsruhe, Germany*
[b] *Department of Meteorology and Geophysics, University of Vienna, Vienna, Austria*
[c] *Department of Meteorology and Bolin Center for Climate Research, Stockholm University, Stockholm, Sweden*

ABSTRACT: Waterbelt climate states with an ice-free tropical ocean provide a straightforward explanation for the survival of advanced marine species during the Cryogenian glaciations (720–635 million years ago). Previous work revealed that stable waterbelt states require the presence of highly reflective low-level mixed-phase clouds with a high abundance of supercooled liquid in the subtropics. However, the high uncertainty associated with representing mixed-phase clouds in coarse-scale general circulation models (GCMs) that parameterize atmospheric convection has prohibited assessment of whether waterbelt states are a robust feature of Earth's climate. Here we investigate whether resolving convective-scale motion at length scales of hectometers helps us to assess the plausibility of a waterbelt scenario. First, we show that substantial differences in cloud reflectivity among GCMs do not arise from the resolved atmospheric circulation. Second, we conduct a hierarchy of simulations using the Icosahedral Nonhydrostatic (ICON) modeling framework, ranging from coarse-scale GCM simulations with parameterized convection to large-eddy simulations that explicitly resolve atmospheric convective-scale motions. Our hierarchy of simulations supports the existence of highly reflective subtropical clouds if we apply moderate ice nucleating particle (INP) concentrations. Third, we test the sensitivity of cloud reflectivity to the INP concentration. In the presence of high but justifiable INP concentrations, cloud reflectivity is strongly reduced. Hence, the existence of stable waterbelt states is controlled by the abundance of INPs. We conclude that explicitly resolving convection can help to constrain Cryogenian cloud reflectivity, but limited knowledge concerning Cryogenian aerosol conditions hampers strong constraints. Thus, waterbelt states remain an uncertain feature of Earth's climate.

SIGNIFICANCE STATEMENT: The purpose of this study is to assess the impact of atmospheric convection and small airborne ice nucleating particles on the reflectivity of mixed-phase clouds over a subtropical ice margin. This is important as these clouds can determine whether the Cryogenian Earth (720–635 million years ago) was in a hard "snowball" state with a fully ice-covered ocean or a habitable waterbelt state with an ice-free tropical ocean. Our results indicate a clear impact of convection but neither confirm nor deny the existence of a waterbelt state since cloud reflectivity depends critically on the abundance of ice nucleating particles. Therefore, a Cryogenian waterbelt scenario remains uncertain, which calls for more comprehensive Earth system modeling approaches in future studies.

KEYWORDS: Atmosphere; Convection; Cloud microphysics; Paleoclimate; Large eddy simulations

1. Introduction

The geological evidence for active tropical ice sheets during the Cryogenian [720–635 million years ago (Ma)] is most commonly explained by the snowball Earth hypothesis, which suggests a globally ice-covered ocean (Kirschvink 1992; Hoffman et al. 1998). Alternative scenarios incorporating waterbelt climate states with an ice-free tropical ocean have been considered (Hoffman et al. 2017; Abbot et al. 2011; Rose 2015; Hyde et al. 2000) because they allow us to easily explain the survival of demosponges before the termination of the Marinoan glaciation (640–635 Ma) (Love et al. 2009). Among the proposed waterbelt scenarios, the so-called Jormungand hypothesis is particularly attractive as it proposes an entire life cycle of the glaciations and rests on well-established atmospheric dynamics and physics (Abbot et al. 2011). However, recent work has shown that the existence of stable

Jormungand–waterbelt states requires the presence of highly reflective low-level mixed-phase clouds at and near the subtropical ice edge (Braun et al. 2022).

Confidence in the representation of clouds in general circulation models (GCMs) is limited and particularly the treatment of mixed-phase clouds in GCMs is highly uncertain (Boucher et al. 2013; McCoy et al. 2015). Uncertainties arise from parameterized small-scale processes associated with, for example, convective motion and aerosol–cloud interactions that cannot be explicitly resolved by GCMs (Boucher et al. 2013). Therefore, global coarse-scale GCMs with horizontal grid spacings $\mathcal{O}(>100)$ km are essential but limited tools in order to assess the plausibility of highly reflective clouds and its stabilizing impact on Jormungand–waterbelt states (Braun et al. 2022). We here investigate whether limited-area high-resolution simulations, which resolve small scales of the atmospheric circulation, help to reduce the uncertainty regarding the reflectivity of mixed-phase clouds during the Cryogenian glaciations.

The Cryogenian glaciations are thought to be initiated by a runaway ice-albedo feedback (Kirschvink 1992; Hoffman et al.

1998, 2017). According to the Jormungand hypothesis, the climate may have stabilized in a waterbelt instead of a snowball state because the runaway ice-albedo feedback weakened when sea ice entered the subtropics (Abbot et al. 2011). In the original formulation of the Jormungand hypothesis by Abbot et al. (2011), the weakening of the ice-albedo feedback is caused by the exposure of relatively dark bare sea ice. In the subtropics, subsidence associated with the Hadley circulation suppresses precipitation, and promotes evaporation of high-albedo snow deposited on sea ice (Abbot et al. 2011). Hence, subtropical sea ice is snow-free and relatively dark.

In Braun et al. (2022) we showed that in addition to dark subtropical sea ice, highly reflective subtropical clouds are required to maintain a stable waterbelt climate. Reflective subtropical clouds additionally weaken the ice-albedo feedback by masking the shortwave radiative signal of the ice-edge movement seen at the top of the atmosphere (TOA). Hence, highly reflective clouds decouple the TOA energy balance of Earth from the ice-edge movement, a phenomenon also observed in present-day Arctic climate (Sledd and L'Ecuyer 2019). We showed that when assuming a low but plausible bare sea ice albedo, the existence of geologically relevant waterbelt states in GCMs is determined by subtropical cloud reflectivity. However, the Cryogenian subtropical cloud reflectivity was found to strongly differ between GCMs. The difference was sufficiently large to allow or to prohibit a stable waterbelt state at high or low simulated cloud reflectivity, respectively. We attributed the differences in cloud reflectivity to differences in the amount of supercooled liquid contained in subtropical low-level mixed-phase clouds. Since these clouds form below the descending branch of the Hadley cell, they are most likely shallow cumulus or stratocumulus clouds.

The dynamical and microphysical processes that determine the abundance of supercooled cloud liquid cannot be explicitly represented in GCMs due to their coarse horizontal grids and rely on parameterizations. This gives rise to substantial uncertainty of the cloud-radiative effect in future climate projections even under modern climate conditions (Boucher et al. 2013; Sherwood et al. 2014; McCoy et al. 2015). Poorly constrained parameters used in parameterizations are usually applied as tuning parameters; that is, they are adjusted within a plausible range in order to reduce biases between the simulated climate and observations of present-day climate (Hourdin et al. 2017). Due to the lack of observations of paleoclimate atmospheric conditions, parameterizations tuned for present-day Earth are often used for paleoclimate simulations, even though this may not be valid (Pierrehumbert et al. 2011; Abbot et al. 2012; Kageyama et al. 2017). In Braun et al. (2022) we showed that the existence of a stable waterbelt climate can be triggered by varying a loosely constrained tuning parameter, which represents the efficiency of the Wegener–Bergeron–Findeisen (WBF) process. The WBF process is an important sink for supercooled liquid in shallow low-level mixed-phase clouds (Korolev et al. 2017). It describes the consumption of supercooled liquid at the expense of growing ice crystals if cloudy air is supersaturated with respect to ice but subsaturated with respect to liquid (Storelvmo and Tan 2015). The efficiency of the WBF process strongly depends on the number of ice crystals

and in turn on the abundance of ice-nucleating particles (INPs) that initiate droplet freezing. Furthermore, the intensity of the WBF process is determined by the intensity of updrafts that are parameterized in global coarse-scale GCMs. Consequently, in GCMs, the necessity to parameterize subgrid updrafts prohibits a judgement whether Cryogenian subtropical clouds were sufficiently reflective to allow stable waterbelt states. Therefore, we investigate here whether resolving hectometer to kilometer scales of atmospheric motion provides more robust insights into Cryogenian subtropical cloud reflectivity.

Resolving small scales of atmospheric motion allows us to reduce, and at scales of hectometers even omit, uncertain convection parameterizations. We make use of this by applying a state-of-the-art two-moment microphysical scheme that directly couples aerosol–cloud interactions to the resolved atmosphere dynamics (Seifert and Beheng 2006; Seifert et al. 2011; Phillips et al. 2008; Hande et al. 2015). The two-moment microphysical scheme further allows us to explicitly consider the abundance of INPs. We here present a hierarchy of global and local simulations that span horizontal grid spacings from 160 km to 300 m with the Icosahedral Nonhydrostatic atmosphere model in numerical weather prediction mode (ICON-NWP; Zängl et al. 2015) and large-eddy mode (ICON-LEM; Dipankar et al. 2015). Additionally, we conduct simulations with different INP concentrations.

Cryogenian aerosol abundance and composition is uncertain. Cryogenian aerosol scenarios cover a wide range and climatic impacts of aerosol have been discussed in the context of snowball Earth initiation (Liu et al. 2021; Feulner et al. 2015; Macdonald and Wordsworth 2017) and termination (Wu et al. 2021; Abbot and Halevy 2010; Abbot and Pierrehumbert 2010; Le Hir et al. 2010), as well as on snowball climate itself (Li and Pierrehumbert 2011; Hoffman 2016). Massive stratospheric aerosol injections through volcanic eruptions were proposed to have cooled Cryogenian climate (Macdonald and Wordsworth 2017). The rise of eukaryotic algae (800–750 Ma) was proposed to have increased biogenic aerosol abundance leading to higher CCN concentrations (Feulner et al. 2015) and a simultaneous increase of biogenic INP concentrations (Wilson et al. 2015). The most widely discussed Cryogenian aerosol species is mineral dust, for which the focus has mainly been on the direct shortwave radiative effect (Liu et al. 2020, 2021; Abbot and Halevy 2010).

The outline of our manuscript is as follows. We describe the applied models and conduct simulations in section 2. Results are organized in three sections. First, we provide a comparison of cloud reflectivity and the conditions for cloud formation in three GCMs (section 3). Second, we use ICON-NWP and ICON-LEM to assess the impact of convection parameterizations on subtropical cloud reflectivity (section 4). Third, we assess the sensitivity of subtropical cloud reflectivity to the abundance of mineral dust acting as INPs in ICON-NWP and ICON-LEM simulations (section 5). We summarize our key results in section 6.

2. Atmospheric models and conducted simulations

In this section we describe the applied atmospheric models and the corresponding simulations. We analyze Cryogenian

TABLE 1. Overview of simulations conducted with the GCMs CAM, ICON-AES, and ICON-NWP; Δ_h is the nominal horizontal grid spacing.

Model	Δ_h (km)	Period (yr)	CO_2 (ppmv)	Ocean	Sea ice
CAM	310	40	10 000	Interactive thermodynamic	Interactive thermodynamic
ICON-AES	160	40	5000	Interactive thermodynamic	Interactive thermodynamic
ICON-NWP	160	5	5000	Prescribed SST	Prescribed SIC with interactive surface temperatures

subtropical mixed-phase clouds and their environment as simulated by the three GCMs CAM, ICON-AES, and ICON-NWP described in section 2a. We further use ICON-NWP together with ICON-LEM to conduct a hierarchy of simulations ranging from coarse $[\mathcal{O}\,(>100)\text{ km}]$ to fine resolution $[\mathcal{O}\,(<1)\text{ km}]$. This is described in section 2b. We describe the simulations to study the sensitivity of cloud reflectivity to the INP concentration in subsection 2c.

a. Simulations with three general circulation models at coarse horizontal resolution

We compare three GCMs: the Community Atmosphere Model v3.1 (CAM; Collins et al. 2004), ICON in climate mode (Atmosphere in the Earth System v1.3.00: ICON-AES), and ICON in numerical weather prediction mode v2.6.1 (ICON-NWP). ICON-AES and ICON-NWP both use the ICON dynamical core but apply different packages of physical parameterizations (Zängl et al. 2015; Giorgetta et al. 2018; Prill et al. 2020). Table 1 provides an overview of the corresponding simulations.

The CAM and ICON-AES simulations were conducted as part of Braun et al. (2022) at a nominal horizontal grid spacing $\Delta_h \approx 310$ km in CAM and $\Delta_h \approx 160$ km in ICON-AES. The simulations were run in aquaplanet setup coupled to a thermodynamic mixed-layer ocean and a thermodynamic sea ice scheme. Specifically, we here analyze simulations with atmospheric CO_2 concentrations of 10 000 ppmv in CAM and 5000 ppmv in ICON-AES. This yields approximately equal annual-mean global ice-edge latitudes in the two models (Braun et al. 2022). The ICON-AES simulation was conducted with the default Rayleigh-damping coefficient and the threshold value for vapor deposition onto ice crystals, $x_{i,\text{thr}} = 5 \times 10^{-6}$ kg m^{-3}, determining the WBF efficiency. This prohibited geologically relevant waterbelt states in ICON-AES (Braun et al. 2022).

In ICON-NWP we also use an aquaplanet setup. However, since we here focus on clouds, we prescribe sea surface temperature (SST) and sea ice cover (SIC) and set the sea ice thickness to a constant value of 0.5 m. Applying prescribed instead of interactive SST and SIC has a negligible impact on the atmospheric circulation (not shown). The sea ice surface temperatures are interactively calculated using the thermodynamic sea ice scheme by Mironov et al. (2012). The sea ice scheme does not keep track of snow deposited on sea ice. Therefore, we prescribe high sea ice albedo values (0.66–0.79) poleward of 18° latitude, and low sea ice albedo values (0.38–0.45) equatorward of 18° latitude, depending on surface temperature similar as for ICON-AES in Braun et al. (2022). As in Braun et al. (2022), we apply a circular orbit

with zero eccentricity and set the solar constant to 94% of today's value. We set the concentration of atmospheric CO_2 to 5000 ppmv.

We conduct the coarse-scale global ICON-NWP simulation with $\Delta_h \approx 160$ km, 47 vertical levels reaching up to 75 km, and a time step of 600 s. We simulate 6 years and exclude the first year from our analysis, which thus spans 5 years. We apply the convection parameterization based on Tiedtke (1989) and Bechtold et al. (2008), the turbulent transfer scheme by Raschendorfer (2001), the Rapid Radiative Transfer Model based on Mlawer et al. (1997), and the two-moment microphysical scheme based on Seifert and Beheng (2006). The microphysical scheme is particularly designed to represent mixed-phase cloud microphysics (Seifert and Beheng 2006). Since this scheme directly couples cloud microphysical processes to resolved atmosphere dynamics, it is intended to be used for $\Delta_h < 3$ km (Prill et al. 2020). Nevertheless, we apply the two-moment microphysical scheme in all ICON-NWP and ICON-LEM simulations to isolate the impact of the convection parameterization on cloud reflectivity.

We apply the two-moment microphysical scheme with the default configuration for heterogeneous ice nucleation, which considers immersion and depositional freezing as parameterized by Hande et al. (2015). This parameterization determines the INP concentration as a function of air temperature and supersaturation with respect to ice. With the default settings, the maximum INP concentration at −20°C is approximately 0.1 L^{-1}. This is a moderate value on present-day Earth, where INP concentrations at −20°C range from 10^{-2} to 10^{2} L^{-1} (Kanji et al. 2017).

For the nucleation of cloud droplets, we also apply the default configuration, which is based on Segal and Khain (2006) and relates the concentration of cloud condensation nuclei (CCN) to height-dependent profiles of condensation nuclei (CN). Given that Cryogenian aerosol conditions are uncertain, we here apply the default settings, which correspond to a continental profile that exhibits considerably higher CN concentrations than expected in marine environments (Segal and Khain 2006). We briefly discuss potential implications of high CCN concentrations in section 4b.

b. Hierarchy of ICON-NWP and ICON-LEM simulations to study the impact of convection

We here provide an overview of our hierarchy of ICON-NWP and ICON-LEM simulations across horizontal resolutions. ICON-LEM (Dipankar et al. 2015; Heinze et al. 2017; Stevens et al. 2020) also uses the ICON dynamical core, which allows us to apply the same dynamical core from coarse to fine resolutions. The hierarchy is summarized in Table 2, and

TABLE 2. Simulation hierarchy across effective horizontal grid spacings Δ_h. The simulation NWP160 is identical to the ICON-NWP simulation listed in Table 1. All simulations listed in this table are conducted with prescribed SST and SIC and apply the two-moment microphysical scheme based on Seifert and Beheng (2006) with the default parameterization for heterogeneous ice nucleation by Hande et al. (2015). Further details concerning the simulations are given in sections 2b and 4.

Simulation	Model	Δ_h (km)	Domain	Period	Convection	Turbulence scheme	Cloud cover
NWP160	ICON-NWP	160	Global	5 yr	Tiedtke–Bechtold	Raschendorfer	Fractional
NWP10	ICON-NWP	10	Global	5 days	Tiedtke–Bechtold	Raschendorfer	Fractional
NWP2.5	ICON-NWP	2.5	LAM	4.5 days	Tiedtke–Bechtold, shallow only	Raschendorfer	Fractional
NWP2.5cex	ICON-NWP	2.5	LAM	1.5 days	Explicit	Raschendorfer	Fractional
LEM0.6	ICON-LEM	0.6	LEM-6°	6 h	Explicit	3D Smagorinsky	All or nothing
LEM0.3	ICON-LEM	0.3	LEM	6 h	Explicit	3D Smagorinsky	All or nothing

further details are given in section 4. We label simulations by the applied model and Δ_h. NWP160 refers to the global ICON-NWP simulation with $\Delta_h = 160$ km described in section 2a.

NWP160 marks the upper end of Δ_h. ICON supports grid refinement, simulations in limited-area mode (LAM), and nested subdomains (Prill et al. 2020). This allows us to conduct simulations with consecutively decreasing Δ_h based on NWP160. These simulations apply 180 vertical levels reaching up to 20 km. From the surface to 4.4-km altitude the layer thickness Δ_v gradually increases from 15 to 70 m with a logarithmic profile. Between 4.4- and 9-km altitude, $\Delta_v = 70$ m. Above that Δ_v gradually increases to 1.3 km. The simulations are configured as NWP160, except when stated otherwise.

We conduct a global ICON-NWP simulation at $\Delta_h = 10$ km (NWP10) with parameterizations for deep, midlevel, and shallow convection. NWP10 spans 7 days, including 2 days of spinup, and is initialized from NWP160. Furthermore, we conduct two ICON-NWP simulations at $\Delta_h = 2.5$ km in LAM over a subtropical subdomain from 2.5° to 22.5°S and spans 25° in longitudinal direction (Fig. A4). In these two simulations, we either parameterize only shallow convection (NWP2.5) or do not parameterize convection at all (NWP2.5cex). The simulation periods are 5 and 2 days for NWP2.5 and NWP2.5cex, respectively, and include a 12-h spinup. The corresponding initial and lateral boundary conditions are derived from NWP10.

We conduct one ICON-LEM simulation at $\Delta_h = 600$ m (LEM0.6) in LAM. The corresponding subdomain spans 6° in latitudinal and longitudinal direction (Fig. A4). We refer to this subdomain as LEM-6°. The simulated period is 13 h, including 7 h of spinup. The initial and lateral boundary conditions are derived from NWP2.5. LEM0.6 contains a nested subdomain with $\Delta_h = 300$ m (LEM0.3), which is centered within the LEM-6° subdomain and spans 5° in latitudinal and longitudinal direction. We refer to this subdomain as the LEM subdomain. In LEM0.6 and LEM0.3 we prescribe constant SST and SIC due to the short simulation period. ICON-LEM assumes the energy-conserving scales of the turbulent spectrum to be explicitly resolved (Dipankar et al. 2015). Hence, ICON-LEM and ICON-NWP differ in the turbulence scheme (Smagorinsky 1963 vs Raschendorfer 2001). ICON-LEM allows us to explicitly resolve convection and use an all-or-nothing grid scale cloud-cover scheme (i.e., a grid cell is either 100% cloudy or cloud-free). In contrast, ICON-NWP uses a fractional cloud-cover scheme.

c. Simulations to study the impact of the ice nucleating particle concentration on cloud reflectivity

To investigate the sensitivity of cloud reflectivity to the INP concentration we apply a parameterization for heterogeneous ice nucleation derived by Phillips et al. (2008) instead of the default configuration. We apply this parameterization assuming that mineral dust is the only INP species available. Using this parameterization, we modify the INP concentration by increasing the number concentration of aerosol particles n_a that potentially become activated to INPs. We conduct three simulations with $\Delta_h = 2.5$ km (NWP2.5x) and $\Delta_h = 600$ m (LEM0.6x), respectively. The NWP2.5x and LEM0.6x simulation setups are identical to NWP2.5 and LEM0.6. The only exceptions are the dust-only INP parameterization and that NWP2.5x simulations are run for only 2 days, including 12 h of spinup. The simulations are summarized in Table 3 and details are given in section 5.

3. Cloud reflectivity in general circulation model simulations

We begin with investigating the differences in subtropical cloud reflectivity between the global coarse-scale GCMs (CAM, ICON-AES, and ICON-NWP).

a. Cloud reflectivity

As discussed in Braun et al. (2022), the different treatment of low-level mixed-phase clouds in CAM and ICON-AES leads to strong differences in subtropical cloud reflectivity around the ice edge (Fig. 1). We quantify cloud reflectivity by

TABLE 3. Simulations with increased mineral dust aerosol number concentration n_a using the parameterization for heterogeneous ice nucleation by Phillips et al. (2008) limited to mineral dust aerosol. Except for the parameterization for heterogeneous ice nucleation and the shorter duration of NWP2.5x simulations, these simulations are configured in the same way as NWP2.5 and LEM0.6 in Table 2.

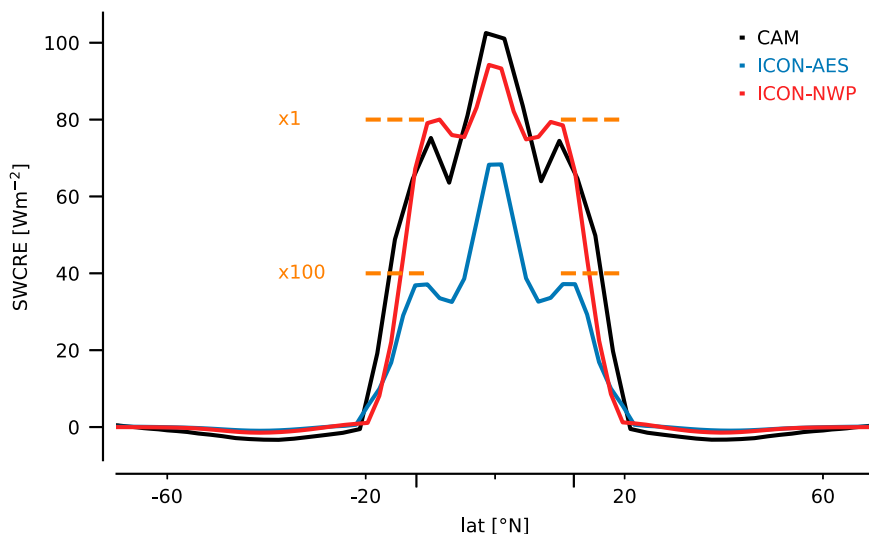| Simulation	Period	n_a (L^{-1})
NWP2.5x1	1.5 days	7×10^2
NWP2.5x10	1.5 days	7×10^3
NWP2.5x100	1.5 days	7×10^4
LEM0.6x1	6 h	7×10^2
LEM0.6x10	6 h	7×10^3
LEM0.6x100	6 h	7×10^4

FIG. 1. Zonal-mean time-mean shortwave cloud-radiative effect (SWCRE) in global simulations with the GCMs CAM, ICON-AES, and ICON-NWP. Analyzed periods comprise 40 years for CAM and ICON-AES and 5 years for ICON-NWP. Longer ticks around 15° latitude indicate the approximate position of the ice edge. The dashed horizontal orange lines indicate estimates of the subtropical SWCRE and the impact of increased ice nucleating particle (INP) concentrations based on NWP2.5x simulations as described in section 5. Here "x1" denotes the SWCRE estimated for the reference INP concentration and "x100" denotes the SWCRE estimated for a high INP concentration.

the shortwave cloud-radiative effect (SWCRE) at the TOA calculated as the difference between all-sky and clear-sky net shortwave radiation.

Low-level cloud tops exhibit temperatures comparable to the surface. Therefore, changes in low-level cloud amount only weakly impact the TOA energy balance via longwave radiation and are negligible regarding the stability of waterbelt states (Braun et al. 2022). Hence, we focus on SWCRE.

The zonal-mean time-mean SWCRE in a waterbelt climate simulated in CAM and ICON-AES is shown in Fig. 1. SWCRE peaks at the equator and exhibits smaller peaks in the subtropics at around 15° latitude. Poleward of 20° latitude SWCRE equals 0 W m^{-2} because of the high albedo of snow deposited on sea ice. In ICON-AES, subtropical SWCRE is about 40 W m^{-2} weaker compared to CAM. As shown in Braun et al. (2022), geologically relevant waterbelt states are promoted by high subtropical SWCRE in CAM and inhibited by the low subtropical SWCRE in ICON-AES.

ICON-NWP exhibits similarly high subtropical SWCRE as CAM (Fig. 1), which supports a Cryogenian waterbelt scenario. However, comparing two GCMs against one GCM is a narrow sample. Thus, no firm conclusions should be drawn as to whether high or low subtropical SWCRE can be considered more realistic. To approach this question, we study the environment of subtropical low-level clouds in the following sections.

b. Cloud controlling factors

We investigate whether the difference in SWCRE among the GCMs arises from differences in the large-scale environment of subtropical clouds. To this end, we study cloud controlling factors (CCFs; see, e.g., Klein et al. 2017). We use as the CCFs

surface temperature T_s, pressure velocity at 500 hPa ω_{500}, and lower-tropospheric stability (LTS) and analyze 5-yr periods based on monthly-mean data. For the CCF analysis, we use a simulation with prescribed SST and SIC for ICON-AES, because for this simulation three-dimensional data are available.

We find that differences in the amount of simulated low-level clouds are not due to differences in the large-scale atmospheric conditions captured by CCFs. This is evident from cloud cover binned by the CCFs and the frequency distributions of the CCFs shown in Fig. 2.

Figures 2a–c show that CAM exhibits substantial low-level cloud cover at all T_s. In ICON-AES substantial low-level cloud cover is limited to 270 K < T_s < 280 K and in ICON-NWP to T_s > 260 K. In contrast to the strong differences in low-level cloud cover, the frequency distributions of T_s similarly exhibit a broad spectrum with low frequency ranging from 220 to 270 K and a distinct peak around 280 K for all GCMs, as shown in Figs. 2d–f.

Figures 2g–i show that CAM and ICON-NWP exhibit low-level clouds at all ω_{500}, whereas in ICON-AES low-level cloudiness is generally weak. For all GCMs the frequency distribution of ω_{500} shows a distinct peak at 0.1 Pa^{-1} (i.e., for subsiding motion in the midtroposphere), which traps clouds in the boundary layer (Figs. 2j–l).

LTS is defined as the difference of potential temperature at 700 hPa and the surface and thus quantifies the strength of the boundary layer inversion, which is an important factor governing the presence of shallow clouds (Wood and Bretherton 2006). All GCMs exhibit the strongest low-level cloud cover for 10 K < LTS < 20 K (Figs. 2m–o). However, CAM exhibits low-level clouds for any LTS. For all GCMs, the frequency
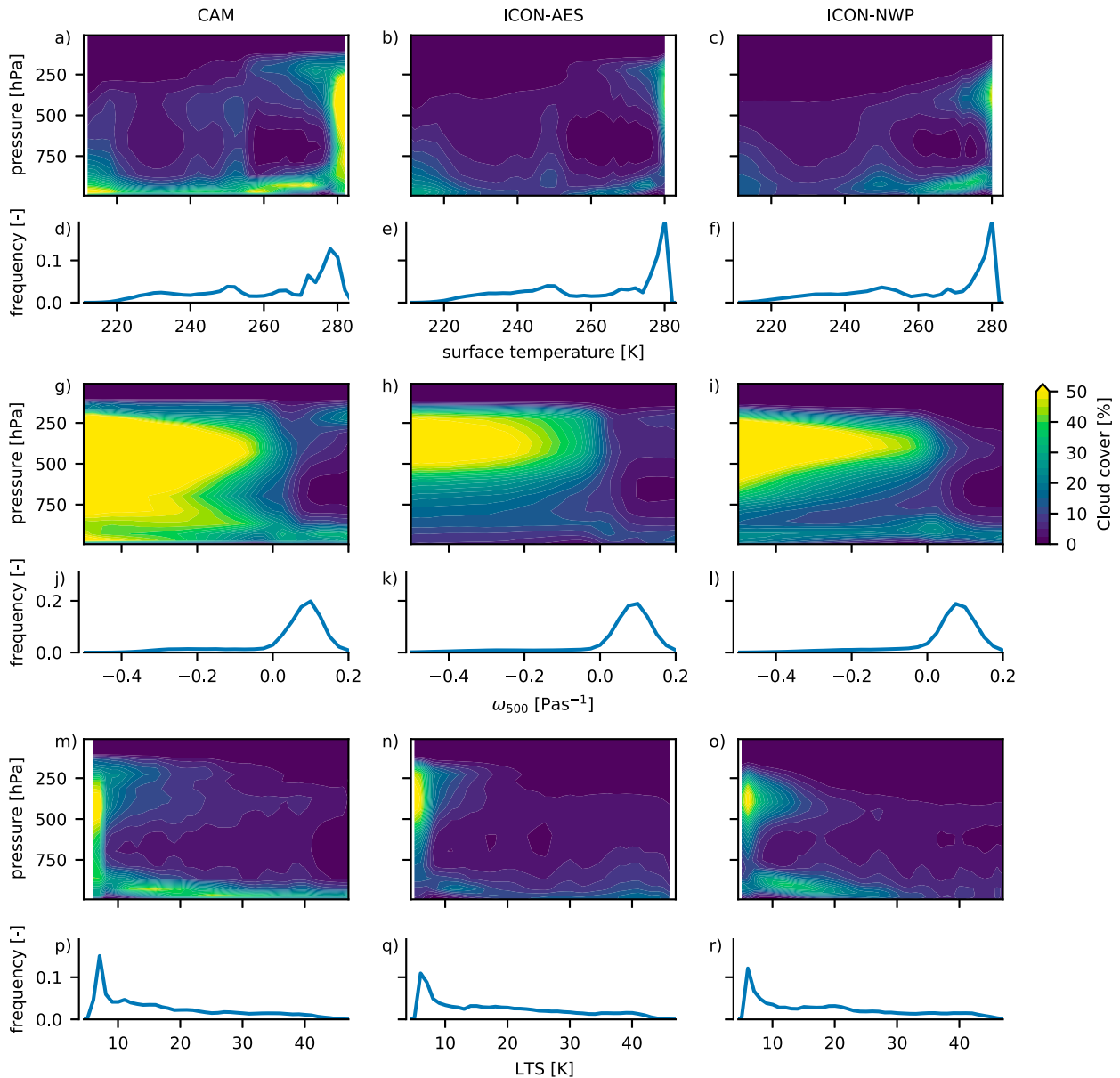
FIG. 2. Cloud cover binned by the cloud controlling factors (CCFs) surface temperature, pressure velocity at 500 hPa ω_{500}, and lower tropospheric stability (LTS) for CAM, ICON-AES, and ICON-NWP and the corresponding distributions of the CCFs. Five-year periods of monthly mean data are used in between $-30°$ and $30°$ latitude.

distribution of LTS exhibits a pronounced peak at very low values and a widespread range of high LTS (Figs. 2p–r).

Overall, the frequency distributions of CCFs exhibit similar shapes and magnitudes in the three GCMs; nonetheless, low-level cloud abundance strongly varies. Hence, the strong SWCRE differences either arise from shorter time scales of the resolved atmospheric circulation or from parameterized sub-grid-scale processes.

c. Synoptic conditions

We study the shorter time scales of the resolved atmospheric circulation by analyzing the synoptic conditions in the subtropical region. We first describe the characteristic synoptic conditions qualitatively and afterward quantify their contribution to the SWCRE.

Qualitatively, subtropical cloud cover in the waterbelt climate simulated in the three GCMs is caused by a combination of large-scale subsidence, leading to shallow cloud formation, and large-scale ascent caused by baroclinic waves. This is evident from the characteristic snapshots of cloud cover and pressure velocity at 850-hPa ω_{850} shown in Fig. 3. We find the following two characteristic features:

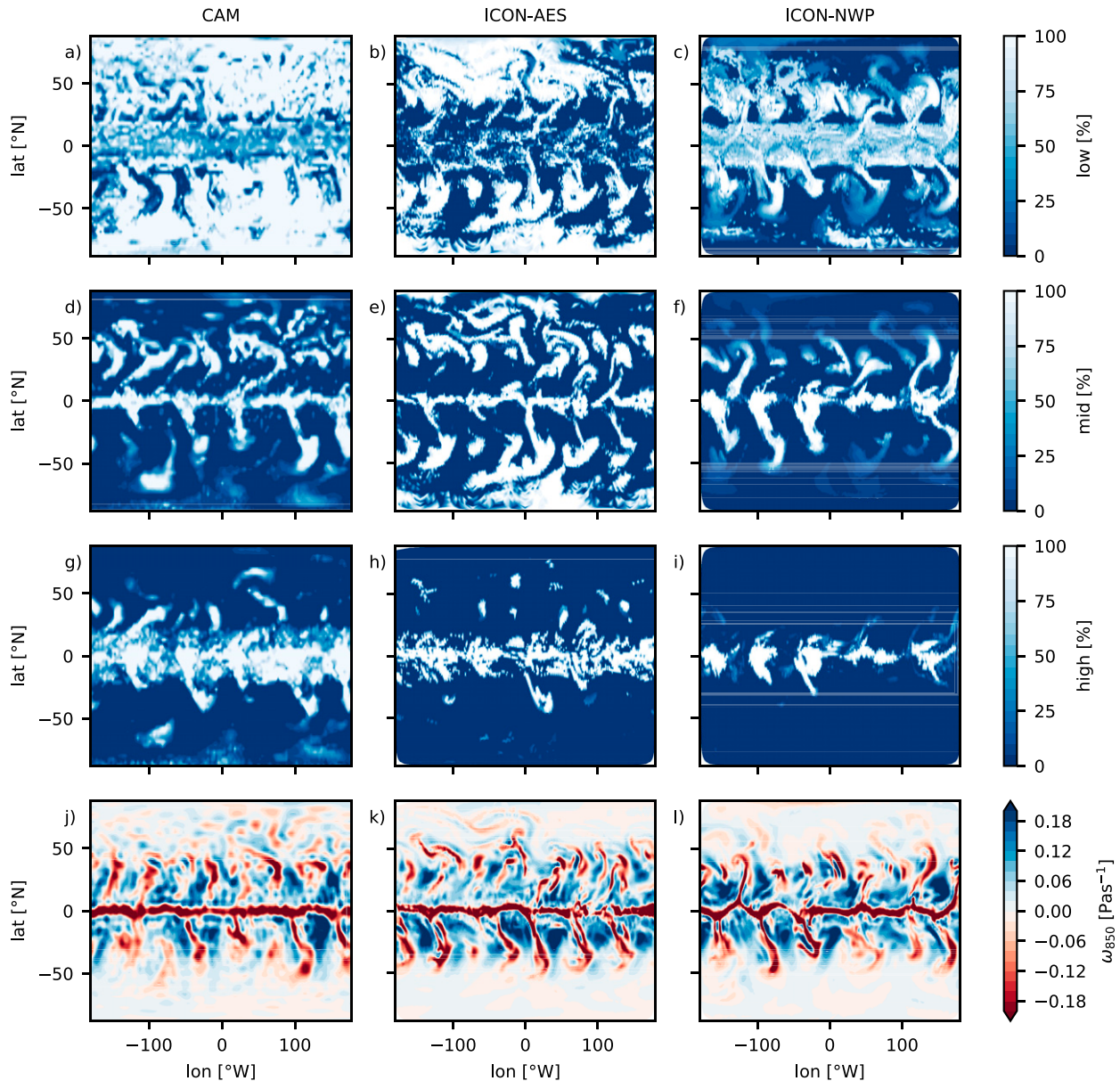1) A pattern of 6–7 branches with intense midlevel cloud cover in each hemisphere extending from the equator into

FIG. 3. Characteristic snapshots of (a)–(i) cloud cover and (j)–(l) pressure velocity at 850 hPa ω_{850} at a single time step during June in CAM, ICON-AES, and ICON-NWP. Clouds below 800 hPa are defined to be low-level clouds (700 hPa in CAM) in (a)–(c), clouds between 800 hPa (700 hPa in CAM) and 400 hPa are defined to be midlevel clouds in (d)–(f), and clouds above 400 hPa are defined to be high-level clouds in (g)–(i).

the extratropics (Figs. 3d–f). The pattern exhibits similarities to the cloud decks observed in warm conveyor belts of extratropical cyclones in present-day climate (Madonna et al. 2014). Note that ω_{850} also shows this pattern, which indicates that these clouds form due to large-scale ascent (Figs. 3j–l). We interpret this as the manifestation of baroclinic waves caused by the strong temperature difference between the warm tropical ocean and the cold extratropical sea ice.

2) Homogeneous low-level cloud cover extending throughout the entire tropics and subtropics (Figs. 3a–c). In ICON-AES, this feature is less pronounced compared to

CAM and ICON-NWP. Figures 3j and 3k show that these homogeneous cloud decks coincide with large-scale subsidence. Large-scale subsidence is caused by the descending branch of the Hadley cell and creates the marine boundary layer inversion, in which shallow low-level clouds form (Wood and Bretherton 2006).

Quantitatively, we find that the three GCMs exhibit similar frequencies of subsidence and ascent, consistent with our CCF analysis. This is shown in Fig. 4a, for which we quantify the contributions of ascent and subsidence to the time-mean
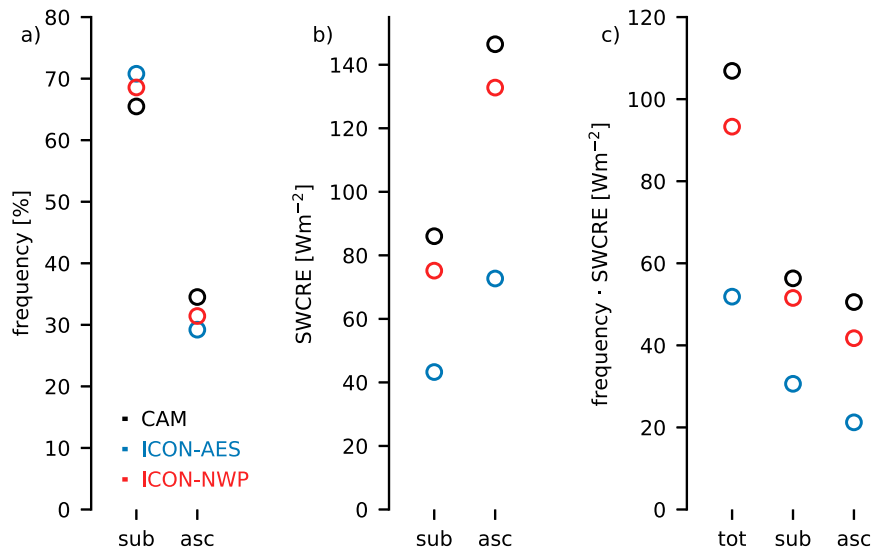
FIG. 4. (a) Frequency of ascent and subsidence, (b) domain-mean time-mean SWCRE for areas of ascent and subsidence, and (c) total domain-mean time-mean SWCRE as well as contributions to total domain-mean time-mean SWCRE from areas of ascent and subsidence. Ascent and subsidence are determined by negative and positive pressure velocity at 850 hPa. The 6-hourly data in the subtropical region (from 22.5° to 2.5°S) during one month (June) from CAM, ICON-AES, and ICON-NWP are used.

domain-mean SWCRE. To do so, we analyze a subdomain spanning 2.5°–22.5°S over a 30-day period based on 6-hourly data. We first exclude all data points without insolation and then filter the data by positive and negative ω_{850}. In the remainder of this manuscript SWCRE refers to the time-mean domain-mean SWCRE.

Figure 4a shows that for all three GCMs the frequency of subsidence at 850 hPa is about 70%. If calculating SWCRE in areas of ascent and subsidence separately, SWCRE is considerably larger for ascent compared to subsidence (Fig. 4b). Figure 4c provides the contributions of areas of subsidence and ascent to the total SWCRE. These contributions are the product of the SWCRE calculated separately for subsidence and ascent (Fig. 4b) and the corresponding frequencies (Fig. 4a). Areas of subsidence and ascent contribute with approximately equal shares to subtropical SWCRE with slightly stronger contributions from areas of subsidence.

In summary, we find that in the three GCMs clouds exist under similar synoptic conditions and CCFs. This reinforces that the SWCRE is sensitive to processes on scales not resolved in coarse-scale GCMs. Therefore, we study the sensitivity of the SWCRE to these unresolved processes (i.e., the treatment of convection and aerosol–cloud interactions) in the following sections.

4. Impact of convection parameterizations

We first investigate whether the high SWCRE found in the global coarse-scale ICON-NWP simulation in section 3a persists in simulations that resolve finer scales of atmospheric motion. To this end, we apply the ICON-NWP and ICON-LEM simulation hierarchy using the moderate default INP concentrations as described in section 2b. The hierarchy

covers horizontal resolutions Δ_h from 160 km to 300 m and gradually downscales the large-scale circulation simulated at $\Delta_h = 160$ km to smaller Δ_h. On the one hand, smaller Δ_h reduces the importance and the requirement of uncertain assumptions associated with convection parameterizations. On the other hand, our simulations at small Δ_h are located within the convective gray zone from $\mathcal{O}\,(10)$ km to $\mathcal{O}\,(10\text{–}100)$ m. On these scales, neither assumption made in convection parameterizations is fully justified, nor is convection fully resolved (Sakradzija et al. 2016). Therefore, we do not consider single simulations to be more realistic than others but instead assess whether different approaches to simulate convection lead to low subtropical SWCRE.

a. ICON-NWP simulations with Δ_h from 160 to 2.5 km

We start by comparing the global coarse-scale ICON-NWP simulation (NWP160) to the global fine-scale ICON-NWP simulation with $\Delta_h = 10$ km (NWP10). In both NWP160 and NWP10, Δ_h is considerably larger than length scales associated with convective plumes. Hence, applying the full convection scheme for shallow, midlevel, and deep convection is reasonable but entails the uncertainties associated with convection parameterizations [e.g., Sherwood et al. (2014)]. At $\Delta_h = 10$ km we only simulate a 5-day period due to the computational cost. We select a representative period as described in section a of the appendix to relate the short period to long-term climate.

We analyze the 5-day period in NWP160 and NWP10 within the tropics and subtropics (from $-30°$ to $30°$ latitude). Figure 5a shows that SWCRE is lower in NWP10 compared to NWP160. The lower SWCRE in NWP10 compared to NWP160 results from less cloud liquid over the ice edge for a similar thermal structure of the atmosphere (Figs. 6a,b) and similar cloud cover (not shown).
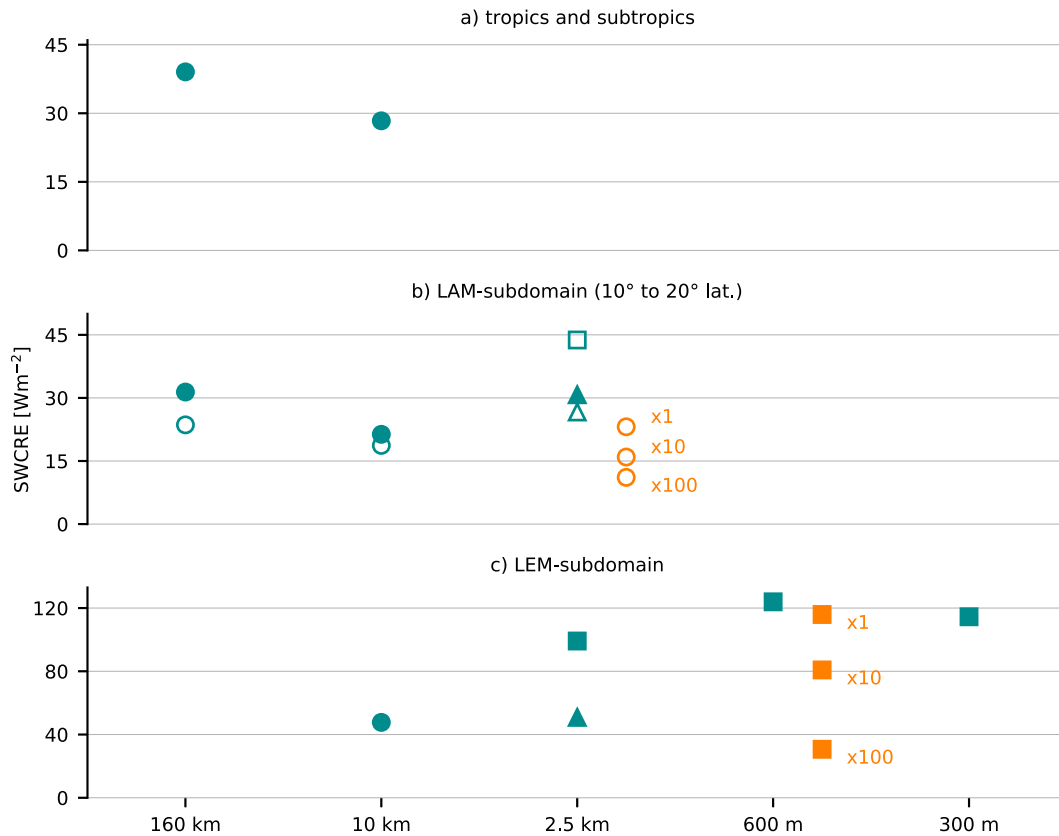
FIG. 5. Domain-mean time-mean shortwave cloud-radiative effect SWCRE determined from (a) a 5-day period for the tropics and subtropics (from $-30°$ to $30°$ latitude), (b) a 4.5-day period in the LAM subdomain (analyzed between $10°$ and $20°$ latitude), and (c) a 6-h period in the LEM subdomain. Circles indicate simulations with parameterizations for shallow, midlevel, and deep convection. Triangles indicate simulations with parameterizations for shallow convection and squares indicate simulations without any convection parameterization. Unfilled markers in (b) indicate data analyzed for a 1.5-day period. Orange markers in (b) and (c) indicate simulations conducted with the heterogeneous ice nucleation parameterization by Phillips et al. (2008), in which mineral dust aerosol is increased by factors of 1, 10, and 100 as discussed in section 5. Note the different scales of the vertical axes.

We apply ICON-NWP in a limited-area mode (LAM) to further decrease Δ_h. At $\Delta_h = 2.5$ km the bulk of convective plumes associated with deep and midlevel convection are explicitly resolved (Weisman et al. 1997). Hence, in NWP2.5 we parameterize shallow convection only. We select the representative LAM subdomain as described in appendix A2. The LAM subdomain contains both shallow low-level clouds and midlevel clouds associated with large-scale ascent. We
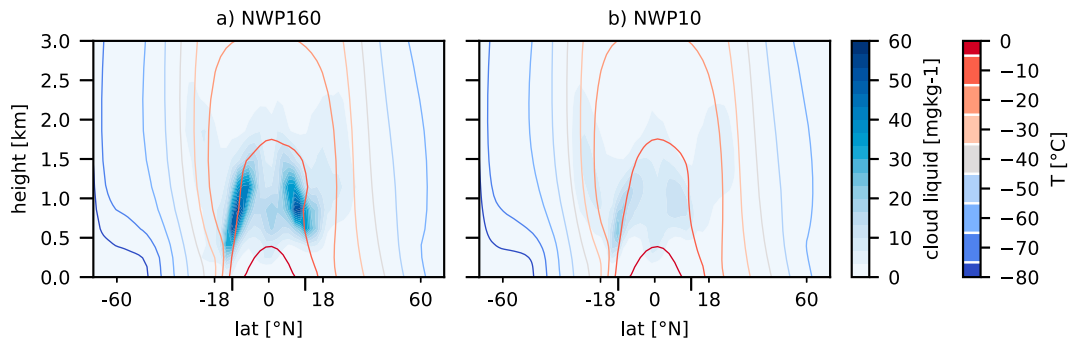

FIG. 6. Zonal-mean time-mean specific cloud liquid mass indicated by shading and isotherms of air temperature T indicated by contours determined from a 5-day period of simulations at (a) $\Delta_h = 160$ km (NWP160) and (b) $\Delta_h = 10$ km (NWP10). Longer ticks indicate the position of the ice edge.
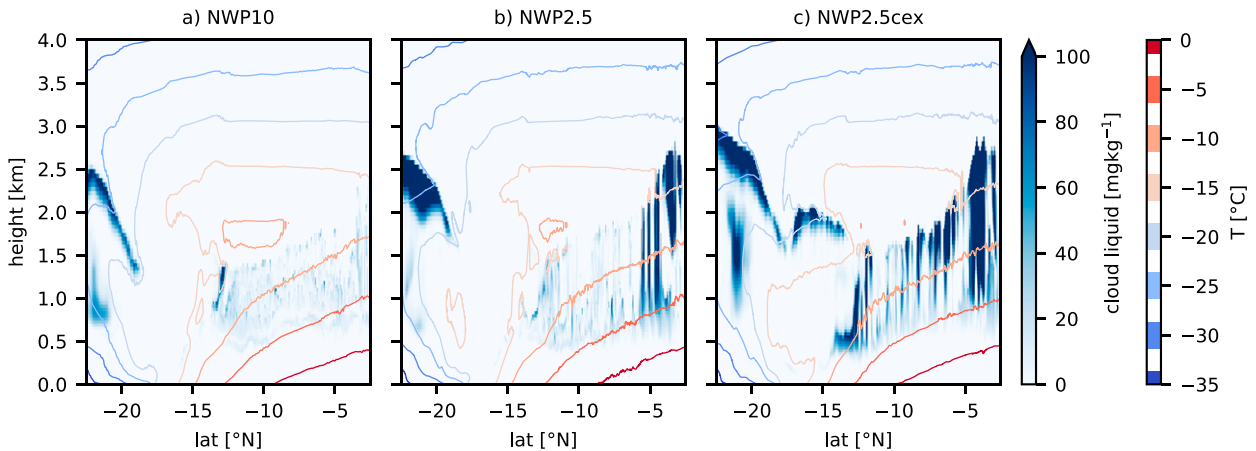
FIG. 7. Meridional cross sections at a single time step at 123° longitude showing specific cloud liquid mass indicated by shading along with isotherms of air temperature T indicated by contours. The ICON-NWP simulations were conducted (a) at $\Delta_h = 10$ km (NWP10), (b) at $\Delta_h = 2.5$ km with parameterized convection (NWP2.5), and (c) at $\Delta_h = 2.5$ km with explicitly resolved convection (NWP2.5cex).

specifically analyze the region between 10° and 20° latitude to focus on clouds close to the ice edge and to exclude near-equatorial deep convective clouds.

Figure 5b compares NWP2.5 with subsets of the simulations NWP160 and NWP10, which we here also analyze over the LAM subdomain in between 10° and 20° latitude for the corresponding period. The reduction of SWCRE with decreasing Δ_h from 160 to 10 km is also evident in the LAM subdomain. Further decreasing Δ_h from 10 to 2.5 km increases SWCRE again. In NWP2.5, SWCRE is as strong as in NWP160. The specific cross sections in Figs. 7a and 7b show that the atmospheric thermal structure is similar in NWP2.5 and NWP10. Yet, NWP2.5 exhibits considerably more cloud liquid than NWP10, which is presumably caused by the stronger updrafts (not shown).

Having $\Delta_h = 2.5$ km challenges the statistical assumptions made in the shallow convection parameterization, because the grid cells may be too small to contain robust samples of convective plumes (Sakradzija et al. 2016). Hence, we conduct an additional simulation with $\Delta_h = 2.5$ km, in which we also turn off the shallow convection parameterization (NWP2.5cex, for "convection explicit"). This omits the limitations of the statistical assumptions in the convection parameterization. However, $\Delta_h = 2.5$ km is too large to resolve the shallow boundary layer convection and sufficiently resolve detrainment via small-scale turbulence (Lebo and Morrison 2015). Nevertheless, simulations at $\Delta_h = 2.5$ km without convection parameterizations have been used to study the sensitivity of cloud-radiative effects to the treatment of convection (see, e.g., Stevens et al. 2020; Hohenegger et al. 2020; Senf et al. 2020).

Turning off the shallow convection parameterization at $\Delta_h = 2.5$ km strongly increases SWCRE. This is evident when comparing NWP2.5cex with the first 1.5 days from NWP160, NWP10, and NWP2.5 on the LAM subdomain (unfilled cyan markers in Fig. 5b). The strong increase of SWCRE is likely caused by underestimated detrainment rates in NWP2.5cex.

Consistently, Fig. 7 shows that in NWP2.5cex cloud liquid is more abundant and more widespread compared to NWP10

and NWP2.5 (i.e., NWP2.5cex exhibits cloud liquid, whereas NWP10 and NWP2.5 do not exhibit any cloud). In Fig. 7 this is the case at −17° latitude at around 2-km altitude. Here, cloud longwave radiative warming alters the thermal structure of the boundary layer compared to NWP2.5 as further discussed in section 4b.

Overall, the high SWCRE found in NWP160 persists if reducing Δ_h in ICON-NWP. NWP10 exhibits lower SWCRE than NWP160 (Fig. 5a) but the difference is much smaller than between ICON-NWP and ICON-AES, where the difference in subtropical SWCRE is 50% (Fig. 1). In the following, we assess whether the high SWCRE persists if we further decrease Δ_h in ICON-LEM simulations.

b. ICON-LEM simulations with Δ_h of 600 m and 300 m

Shallow boundary layer clouds are stronger impacted by hectometer-scale convective processes than clouds associated with the large-scale ascent caused by cyclonic events. Therefore, we focus our ICON-LEM simulations on a shallow cloud deck over the ice edge.

We conduct ICON-LEM simulations in LAM with $\Delta_h = 600$ m (LEM0.6) and simultaneous online one-way grid nesting with $\Delta_h = 300$ m (LEM0.3). We select a suitable subdomain for LEM0.6 as described in section A3. A large fraction of this subdomain is covered by low-level clouds (Figs. 8a,b). Midlevel clouds caused by large-scale ascent are only present in the southwest corner of the subdomain (Figs. 8c,d). High-level cloud cover is negligible (not shown).

We assume that convection is explicitly resolved in LEM0.6 and LEM0.3. On the one hand, large-eddy simulations with $\Delta_h = 300$ are far from resolving length scales $\mathcal{O}(10)$ m required for an accurate explicit simulation of shallow clouds (Stevens et al. 2002). On the other hand, the largest convective eddies within the boundary layer exhibit length scales on the order of the boundary layer height, which is about 1.8 km in our simulations. Hence, the large scales of the boundary layer circulation can be represented in LEM0.6 and LEM0.3.
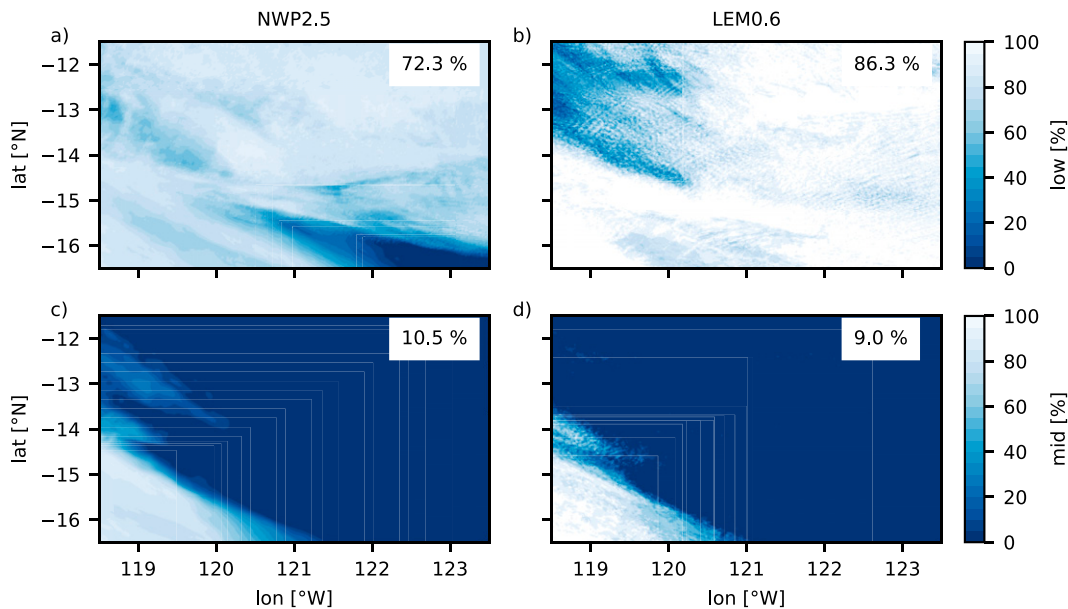
FIG. 8. (top) Low-level and (bottom) midlevel cloud cover averaged over 6-h periods over the LEM subdomain in simulations (a),(c) NWP2.5 and (b),(d) LEM0.6.

Figure 5c compares SWCRE from LEM0.6 and LEM0.3 on the LEM subdomain LEM with simulations NWP10, NWP2.5, and NWP2.5cex, which we here analyze over the same subdomain and the corresponding period. SWCRE in LEM0.6 and LEM0.3 is higher than in NWP2.5cex and exceeds SWCRE in NWP2.5 and NWP10 by more than 100%.

The differences between NWP2.5, NWP2.5cex, LEM0.6, and LEM0.3 are analyzed in Fig. 9 by means of time-mean domain-mean vertical profiles. The profiles of specific humidity q_v indicate that the shallow boundary layer clouds are supplied with moisture from the surface (Fig. 9a). The near-surface increase of relative humidity (Fig. 9b) at constant q_v indicates adiabatic cooling. Beyond 400-m altitude cloud liquid and ice forms consuming q_v. The top of the boundary layer at around 1.8-km height is marked by the strong decrease of q_v and the increase of equivalent potential temperature θ_e (Fig. 9c). The dry, warm air aloft is caused by large-scale subsidence. Although the q_v profiles exhibit a similar structure, the profiles of cloud liquid and ice differ substantially in magnitude and shape (Figs. 9d,e).

LEM0.6 and LEM0.3 exhibit high amounts of cloud liquid while NWP2.5 and NWP2.5cex exhibit high amounts of cloud ice. This is consistent with more intense updrafts in ICON-LEM (Fig. 9f). We calculate updraft intensity as the domain-mean time-mean over all grid points with upward velocity. Higher updraft intensity leads to higher relative humidity in between 0.5- and 1.5-km altitude (Fig. 9b), which facilitates the formation of cloud liquid. However, the higher updraft intensity in LEM0.3 compared to LEM0.6 does not lead to higher amounts of cloud liquid, indicating stronger detrainment in LEM0.3.

The shapes of the vertical profiles point toward different dominant cloud types. In ICON-LEM, the approximately linear increase of cloud liquid with altitude and the constant

relative humidity between 0.5- and 1.5-km altitude indicate liquid water production at low lateral dry air entrainment rates. This suggests stratocumulus clouds as the dominant cloud type (Rauterkus and Ansorge 2020). In contrast, the relatively constant profiles of cloud liquid in NWP2.5 and NWP2.5cex indicate considerable lateral entrainment. This suggests dominance of shallow cumulus clouds (de Rooy et al. 2013).

NWP2.5 exhibits particularly low cloud liquid and a pronounced peak of cloud ice below 1-km altitude (Fig. 9). This may be caused by an amplifying feedback of reduced longwave surface warming leading to reduced surface temperatures and reduced surface moisture supply.

NWP2.5cex exhibits a pronounced peak of cloud liquid and ice above the boundary layer at 2-km altitude (Fig. 9d). As discussed in section 4a, detrainment rates are likely underestimated in NWP2.5cex, which may allow convective shafts to penetrate into the free troposphere (Lebo and Morrison 2015). The associated excessive cloud liquid formation warms the boundary layer as shown in Fig. 7. This weakens the boundary layer inversion as is evident from the θ_e profile in Fig. 9c, which additionally facilitates cloud formation above the boundary layer.

Overall, our hierarchy across horizontal resolutions indicates that the treatment of convection considerably impacts subtropical Cryogenian SWCRE, especially within the gray zone of convection. The strong impact of convection treatment was also reported in studies of present-day climate (Stevens et al. 2020; Senf et al. 2020). Even though all our simulations have limitations concerning the representation of convection, we find that the dynamical environment of shallow low-level clouds allows a high subtropical SWCRE irrespective of the specific treatment of convection.
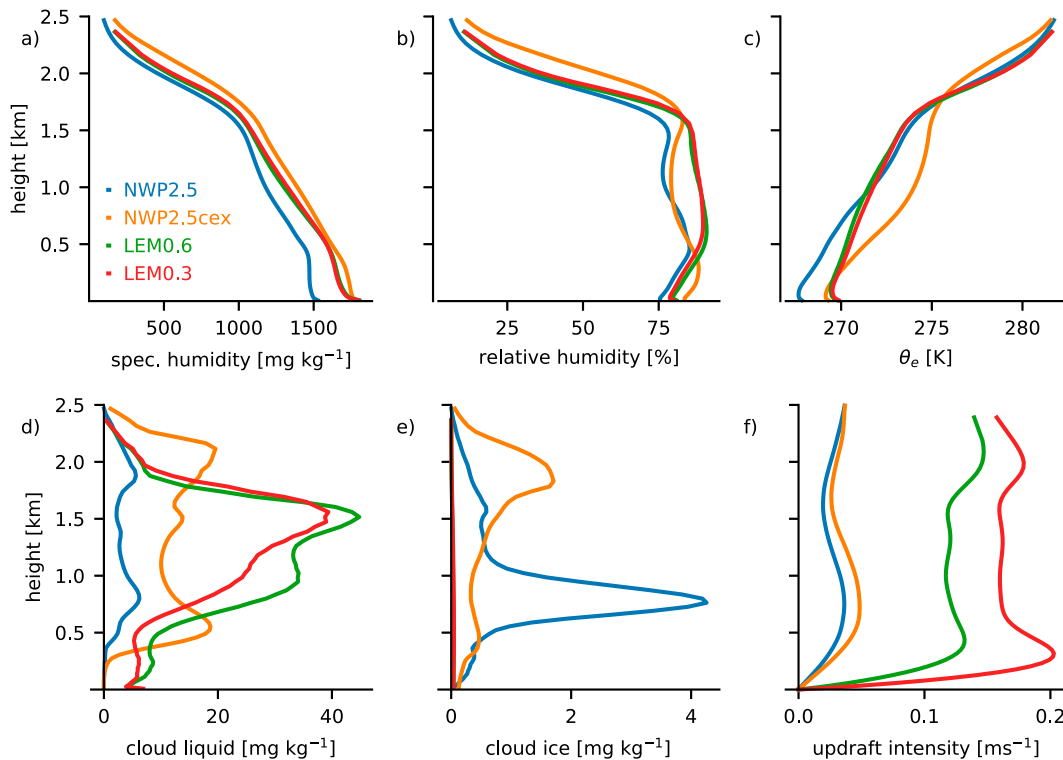
FIG. 9. Domain-mean time-mean vertical profiles of (a) specific humidity, (b) relative humidity, (c) equivalent potential temperature θ_e, (d) specific cloud liquid, (e) specific cloud ice, and (f) updraft intensity determined from a 6-h period on the LEM subdomain for ICON-NWP simulations at Δ_h = 2.5 km with shallow convection parameterized (NWP2.5) and explicitly resolved (NWP2.5cex) and ICON-LEM simulations at Δ_h = 600 m and Δ_h = 300 m (LEM0.6 and LEM0.3).

We point out that both the INP concentration and the CCN concentration are expected to impact SWCRE. The high SWCRE in our hierarchy of simulations is found using the default INP and CCN configurations of ICON, which represent moderate INP concentrations and fairly high CN and thus CCN concentrations. In marine environments, CCN concentrations may be considerably lower than what is assumed here (Segal and Khain 2006). According to Twomey (1977), low CCN concentrations lead to fewer and larger cloud droplets and thus weaker SWCRE. However, we here focus on the impact of varying the INP concentration, which we study in section 5.

5. Sensitivity of cloud reflectivity to the abundance of ice nucleating particles

In this section we investigate the sensitivity of cloud reflectivity to the abundance of INPs. We here choose to focus on a scenario considering high abundance of mineral dust aerosol and study its impact on ice formation and the WBF process.

a. Cryogenian mineral dust ice nucleating particles

During the Cryogenian, soil erodibility likely was high due to the absence of land plants (Morris et al. 2018; Liu et al. 2020). Liu et al. (2020) conducted GCM simulations of

temperate Cryogenian climate with interactive dust aerosol and assuming high soil erodibility. They found a global-mean atmospheric dust loading up to 40 times higher than in present-day climate. Model estimates by Abbot and Halevy (2010) assuming a snowball climate even suggest that atmospheric dust loading was 100 times higher than in present-day climate. Given that mineral dust aerosols are the dominant ice-nucleating species in present-day climate (Kanji et al. 2017), we neglect all ice-nucleating species except mineral dust. To do so, we apply the heterogeneous ice nucleation parameterization by Phillips et al. (2008), referred to as the dust-only parameterization, instead of the default parameterization by Hande et al. (2015). This allows us to explicitly set the number concentration of specific aerosol species for heterogeneous ice formation. To isolate the impact of modifying the INP concentration, we leave the treatment of CCN unchanged.

The dust-only heterogeneous ice nucleation parameterization includes immersion and depositional freezing. It considers a constant, homogeneous aerosol number concentration n_a. The INP concentration is determined by n_a, air temperature, and supersaturation with respect to ice. We set $n_a = 0$ for all aerosol species except mineral dust and assume a reference dust aerosol concentration $n_a = 700\ \text{L}^{-1}$. This assumption results in a maximum INP concentration at $-20°\text{C}$ on the order of $1\ \text{L}^{-1}$, which is roughly the median of values
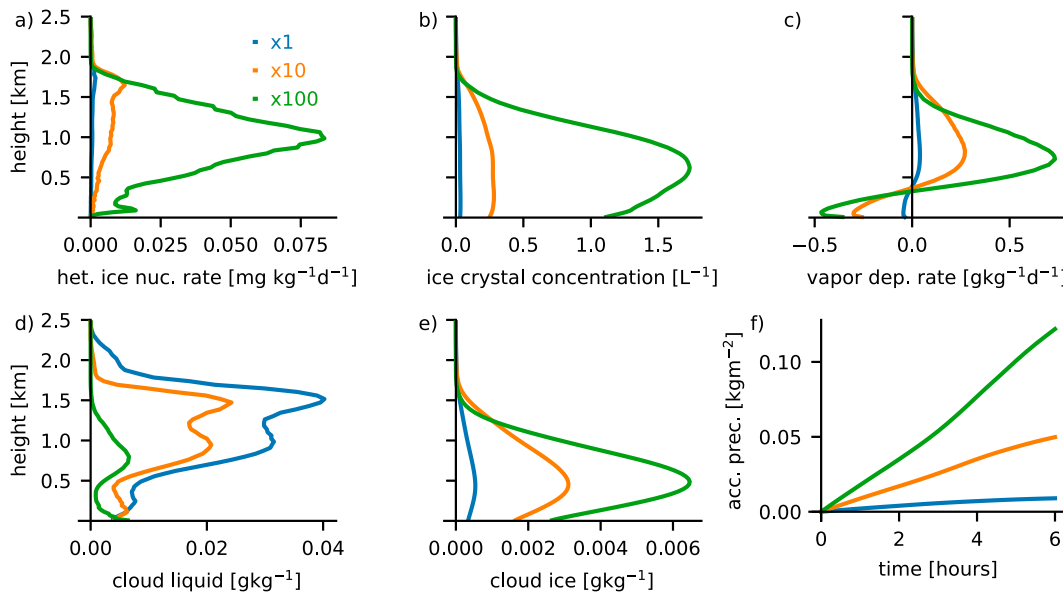
FIG. 10. Domain-mean time-mean profiles of (a) heterogeneous ice nucleating rate, (b) ice crystal number concentration, (c) rate of vapor deposition onto ice crystals, (d) specific cloud liquid, (e) specific cloud ice, and (f) accumulated precipitation at the surface in ICON-LEM simulations with concentrations of ice nucleating particles increased by factors of 1, 10, and 100 (simulations LEM0.6x). Data are analyzed for a 6-h period over the LEM subdomain.

expected on present-day Earth (Kanji et al. 2017). At $-20°C$ the dust-only parameterization yields a higher maximum INP concentration than the default parameterization by Hande et al. (2015), for which the maximum concentration is 0.1 L^{-1} at the same temperature. However, the variation of the INP concentration with air temperature and supersaturation differs between the two parameterizations and the dust-only parameterization does not necessarily result in an overall higher atmospheric abundance of INPs. For our purposes it is important to note that the transition from the default heterogeneous ice nucleation parameterization to the dust-only parameterization only weakly affects SWCRE at $\Delta_h = 2.5$ km and 600 m. This is shown by the cyan and orange marker labeled by "x1" in Figs. 5b and 5c.

Given the high estimates of the global-mean atmospheric dust loading under Cryogenian conditions we increase n_a by factors of 10 and 100. If the atmospheric state is the same, increasing n_a by a factor of 100 leads to an INP concentration of 100 L^{-1} at $-20°C$. This is an extreme value under present-day climate conditions, but in our opinion justifiable given under Cryogenian conditions.

b. Simulations with increased concentrations of mineral dust ice-nucleating particles

We investigate the impact of increasing the INP concentration on SWCRE using ICON-NWP at $\Delta_h = 2.5$ km with parameterized shallow convection over the LAM subdomain (simulation set NWP2.5x) and ICON-LEM at $\Delta_h = 600$ m over the LEM subdomain (simulation set LEM0.6x). This allows us to investigate the sensitivity of SWCRE to INP concentrations for different synoptic conditions and different treatments of convection. For each set of simulations we

conduct a reference simulation with $n_a = 700$ (referred to as x1) and simulations with n_a increased by factors of 10 (x10) and 100 (x100).

We first investigate the impact of increasing the INP concentration using the set of LEM0.6x simulations and the corresponding time-mean domain-mean vertical profiles shown in Fig. 10. An increased INP concentration leads to an increased heterogeneous ice formation rate, which is dominated by immersion freezing in mixed-phase clouds (Kanji et al. 2017). More intense heterogeneous ice nucleation leads to a larger ice crystal number concentration, which enhances water vapor deposition onto ice crystals at altitudes above 400 m (Fig. 10c). In contrast, at altitudes below 400 m, ice crystals sublimate due to the relatively low relative humidity in the below-cloud layer (cf. Fig. 9b). The enhanced vapor deposition above 400 m indicates enhanced liquid-ice conversion via the WBF process, which strongly depletes liquid at the expense of ice. In our current model setup, ice crystals have a larger terminal fall speed and tend to precipitate more easily than rain drops. Hence, accumulated precipitation at the surface increases (Fig. 10f) and total cloud condensate decreases. Overall, cloud liquid strongly decreases with larger INP concentrations. Sublimation and vapor deposition impact the size of ice crystals. However, changes in the ice crystal size are not considered in the radiation scheme. Thus, the changes in cloud liquid determine the impact of the cloud microphysical processes on SWCRE.

The strong decrease of cloud liquid with increasing INP concentration leads to a strong decrease in SWCRE in the LEM0.6x simulations as shown in Fig. 11 and the orange markers in Fig. 5c. SWCRE decreases by more than 90 W m^{-2} when increasing n_a by a factor of 100. This is a relative
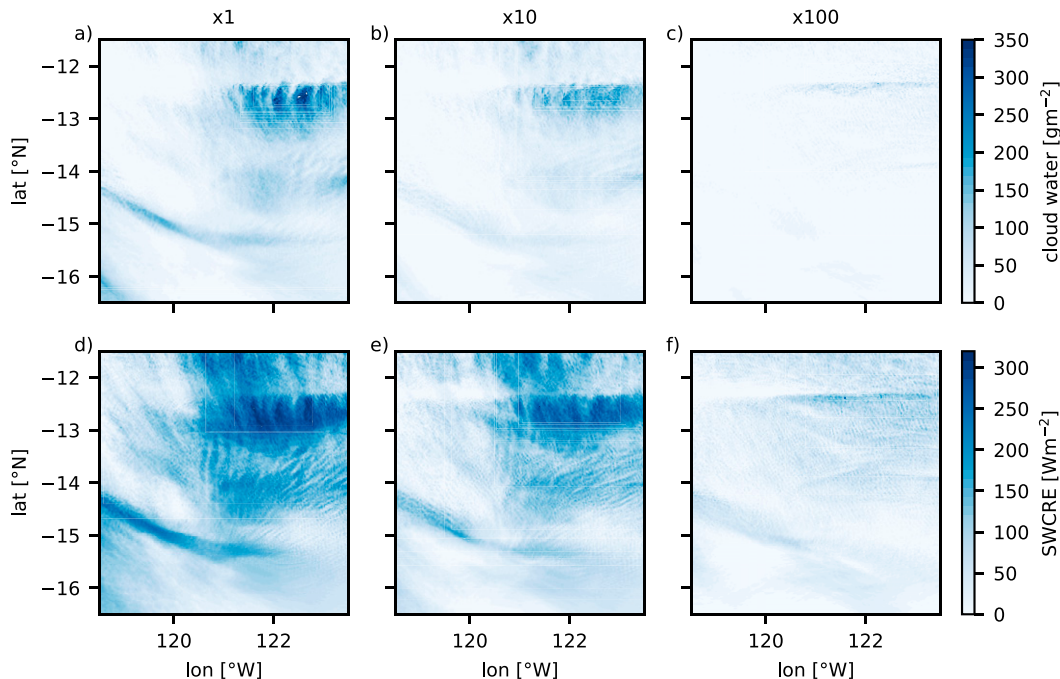
FIG. 11. (top) Vertically integrated cloud liquid and (bottom) shortwave cloud-radiative effect (SWCRE) at the top of the atmosphere (TOA) averaged over 6-h periods over the LEM subdomain in ICON-LEM simulations with increased concentrations of ice nucleating particles: (left) LEM0.6x1, (middle) LEM0.6x10, and (right) LEM0.6x100.

SWCRE decrease by more than 75%. This decrease exceeds the differences found in SWCRE due to the treatment of convection found in Fig. 5. We also find a decrease of SWCRE in ICON2.5x simulations on the LAM subdomain (Fig. 5b). The absolute decrease of SWCRE in ICON2.5x is considerably smaller compared to LEM0.6x, because NWP2.5 exhibits less cloud liquid than LEM0.6. However, SWCRE decreases by 50% if comparing NWP2.5x1 with NWP2.5x100, which is as large as the differences found due to the treatment of convection (Fig. 5b).

Overall, we find that SWCRE is strongly reduced in the presence of high INP concentrations. This holds for NWP2.5x and LEM0.6x, which represent different synoptic conditions and parameterize and resolve shallow convection, respectively. Our results are in agreement with simulations of mixed-phase stratocumulus and cumulus clouds under present-day climate conditions by Vergara-Temprado et al. (2018). These clouds are located in the cold sector of extratropical cyclones over the Southern Ocean. Based on simulations with 2-km horizontal grid spacing, Vergara-Temprado et al. (2018) estimated that SWCRE could range from 42 to 105 W m^{-2} due to variations of the INP concentration. In present-day climate the abundance of mineral dust aerosol over the Southern Ocean is generally low due to the large distance to continental regions (Vergara-Temprado et al. 2018). Consistently, the impact of particularly varying mineral dust aerosol concentrations on stratiform mixed-phase clouds over the Southern Ocean is low under present-day climate conditions (McGraw et al. 2020). However, Sagoo and Storelvmo (2017) stated a significant impact of mineral dust aerosol on

the SWCRE of mixed-phase clouds in simulations with climatic conditions representing the last glacial maximum 20 000 years before the present.

The high sensitivity of SWCRE to INP concentrations in our simulations implies that high INP concentrations may hamper the existence of stable waterbelt states. This is evident if we estimate the impact of the high sensitivity of SWCRE to INP concentrations on the global scale as indicated by the dashed orange lines in Fig. 1. The estimate is based on two assumptions. First, we assume that SWCRE in the subtropical region is as high as in NWP160 if using the reference dust-only INP concentration. This assumption is supported by the equal SWCRE in NWP2.5x1 and NWP160 shown in Fig. 5b. We approximate subtropical SWCRE for the reference case to be 80 W m^{-2} (dashed orange line x1 in Fig. 1). Second, we assume that the 50% reduction of SWCRE with increasing n_a by 100 found in 2.5x simulations (x1 vs x100 in Fig. 5b) is representative for the entire subtropical region. This assumption is based on our choice of representative subdomains and periods. Applying the 50% reduction of SWCRE yields a subtropical SWCRE of 40 W m^{-2} (x100 in Fig. 1). This is close to the SWCRE found in ICON-AES, for which climate does not stabilize in a waterbelt state (Braun et al. 2022). Hence, high but still plausible INP concentrations may hamper the existence of waterbelt states. As a consequence, the existence of stable waterbelt states may be determined by the abundance of mineral dust aerosol.

However, the abundance and distribution of mineral dust aerosol during the initiation of the Cryogenian glaciations is highly uncertain, as it is determined by several factors. First,

despite the absence of land vegetation, crust formation potentially leads to low soil erodibility (Liu et al. 2020). Second, the distribution of INPs likely exhibited high spatial variability. GCM simulations by Liu et al. (2020) indicated that Cryogenian maritime regions, where the impact of INPs on shallow mixed-phase cloud reflectivity is crucial, exhibited low dust aerosol concentrations. Third, on the way toward a snowball climate, the extent of land glaciers, which strongly depends on topography (Rodehacke et al. 2013; Walsh et al. 2019), determined the continental area emitting dust. Fourth, dust may sediment into sea ice at high latitudes and subsequently be transported within the sea ice toward the equator (Hoffman 2016). Accordingly, mineral dust might be exposed due to surface net evaporation in the subtropical region, just in the right spot to impact cloud reflectivity above the ice edge.

Given our limited knowledge concerning Cryogenian aerosol scenarios, varying aerosol concentrations by a factor of 100 in our view is justified. The corresponding differences in SWCRE are equal to or even exceed the differences arising from the treatment of convection. Hence, even if convection and turbulence were properly represented in the model simulations, limited knowledge concerning Cryogenian aerosol composition and abundance precludes a robust judgement of the plausibility of waterbelt scenarios.

6. Conclusions

The existence of stable Cryogenian waterbelt states requires that subtropical low-level mixed phase clouds be highly reflective (Braun et al. 2022). Here we investigate to what extent the cloud reflectivity depends on the treatment of convection and the assumed concentration of ice nucleating particles (INPs). In particular, we seek if high-resolution models with explicit convection support highly reflective clouds, and how this is modulated by INPs.

We show that the radiative properties of Cryogenian mixed-phase clouds are governed by processes that are strongly parameterized in coarse-scale general circulation models (GCMs) such as convection and aerosol–cloud interactions. High-resolution simulations allow us to explicitly resolve convective-scale motions and improve the representation of aerosol–cloud interactions. We gradually reduce the dependency on parameterized subgrid-scale processes through a hierarchy of simulations ranging from horizontal grid spacings of 160 km to 300 m assuming moderate INP concentrations. In particular our large-eddy simulations with explicitly resolved convection promote a high abundance of supercooled liquid and thus highly reflective clouds. Although we find that cloud reflectivity depends on the treatment of convection, the hierarchy of simulations overall supports highly reflective subtropical clouds.

We further study the impact of increasing the INP concentration from moderate to high plausible values under Cryogenian conditions. Increasing the INP concentration enhances the Wegener–Bergeron–Findeisen process and strongly reduces supercooled liquid. The associated reduction of cloud reflectivity is larger than the differences found due to the treatment of convection. The high sensitivity of cloud reflectivity to the INP concentration indicates that the existence of stable waterbelt

states may be determined by the abundance of mineral dust aerosol. This extends the importance of mineral dust aerosol for Cryogenian climate beyond its direct radiative effect (Abbot and Halevy 2010; Liu et al. 2020, 2021).

Cryogenian aerosol conditions and the associated impact on cloud reflectivity are highly uncertain. In general, cloud microphysical processes strongly impact cloud reflectivity. Thus, poorly constrained microphysical processes not addressed in this study, such as cloud droplet formation (Lee et al. 2013), secondary ice formation (Field et al. 2017), and the nucleation efficiency of INPs (Hoose and Möhler 2012), add to the cloud uncertainty. Therefore, we cannot constrain Cryogenian cloud reflectivity to either high or low values, and either the presence or the absence of waterbelt states in the real climate system remains possible.

Given the high sensitivity of cloud reflectivity to the treatment of convection and the abundance of INPs, constraining Cryogenian cloud reflectivity requires simulations at relatively high resolutions as well as extending our knowledge regarding the treatment of cloud microphysical processes and Cryogenian aerosol conditions. Advanced estimates of Cryogenian aerosol conditions require comprehensive Earth system models. Tools that may provide the basis for a convergence of Earth system modeling and high-resolution simulations are convection-permitting regional climate models (Giorgi 2019), which could incorporate interactive treatment of aerosol (Drugé et al. 2021). Such advanced model setups appear to be technically feasible in the near future. However, given the substantial uncertainties associated with aerosol–cloud interactions even in present-day climate (Boucher et al. 2013), we doubt that satisfactory constraints on cloud reflectivity will emerge from this approach. Instead we suggest to investigate how other components of the Earth system, such as continents, ocean heat transport, and sea ice dynamics, impact the viability of the Jormungand hypothesis. Comparing their impact to the stabilizing effect of high subtropical cloud reflectivity may reveal whether further advancing our understanding of Cryogenian clouds is indeed crucial.

So far, the Jormungand–waterbelt scenario remains an uncertain explanation for the Cryogenian glaciations. The uncertainty not only exists in coarse-scale GCMs due to uncertain tuning parameters, but persists in hectometer-scale large-eddy simulations with reduced model assumptions. Here, the uncertainty associated with Cryogenian aerosol conditions hampers a judgement whether Earth's climate may have settled in a waterbelt state. Thus, with the current state of knowledge we consider the more robust classical snowball Earth scenario a more likely explanation for the Cryogenian glaciations.
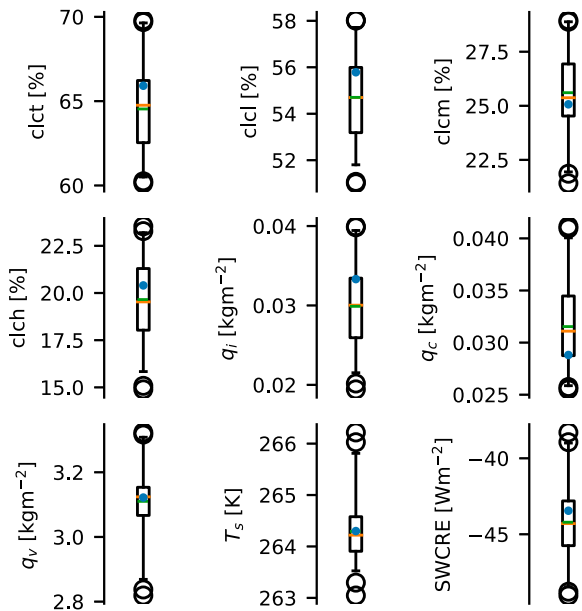
FIG. A1. Distribution of domain-mean time-mean values of 125 5-day periods determined from simulation NWP160. The chosen representative period is marked by the blue dot. This period starts at 11 June in year 5 of the simulation NWP160. The considered variables are total cloud cover (clct), low-, mid-, and high-level cloud cover (clcl, clcm, clch), column cloud ice q_i and liquid q_c, column water vapor q_v, surface temperature T_s, and shortwave cloud-radiative effect SWCRE. The box extends from the lower to upper quartile, and the orange line depicts the median. The green dashed line indicates the mean. The whiskers indicate the 1st and 99th percentiles. Circles indicate outlier points beyond the whiskers.

Data availability statement. The data, corresponding run scripts, and the custom computer code used to generate the results that support the findings of this study are available at https://doi.org/10.5445/IR/1000147858.

APPENDIX

Selection of Representative Periods and Subdomains

We describe the selection of the representative periods and subdomains in the first three subsections and provide an overview of the subdomains in the final subsection.

a. Selection of a 5-day period for NWP10

The annual cycle of global-mean low-level cloud cover in NWP160 peaks at solstice (not shown). Furthermore, our simulation setup is symmetric across the equator.
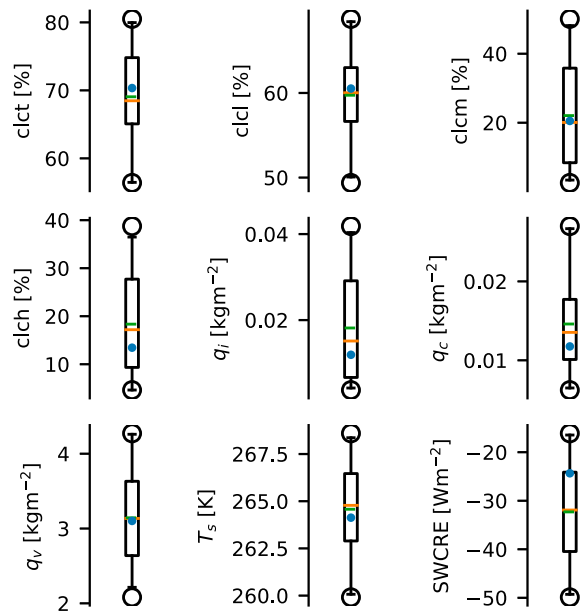
FIG. A2. Distribution of domain-mean time-mean values over 68 subdomains determined from simulation NWP10 for a 4.5-day period. The chosen representative period is marked by the blue dot. For further description see Fig. A1.

Therefore, we choose a 5-day period for the subdomain spanning 2.5°–22.5°S during June. We focus on the winter hemisphere because the ice edge is here closer to the equator than during summer.

We analyze 5-day periods starting on each day between 1 and 25 June of 5 consecutive years from NWP160. This
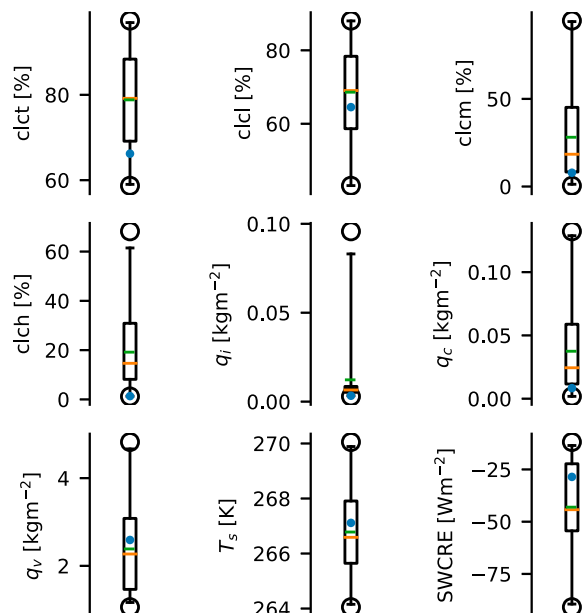

FIG. A3. Distribution of domain-mean time-mean of 80 ensemble members determined from simulation NWP2.5 for 1-day periods. The chosen period is marked by the blue dot. For further description see Fig. A1.
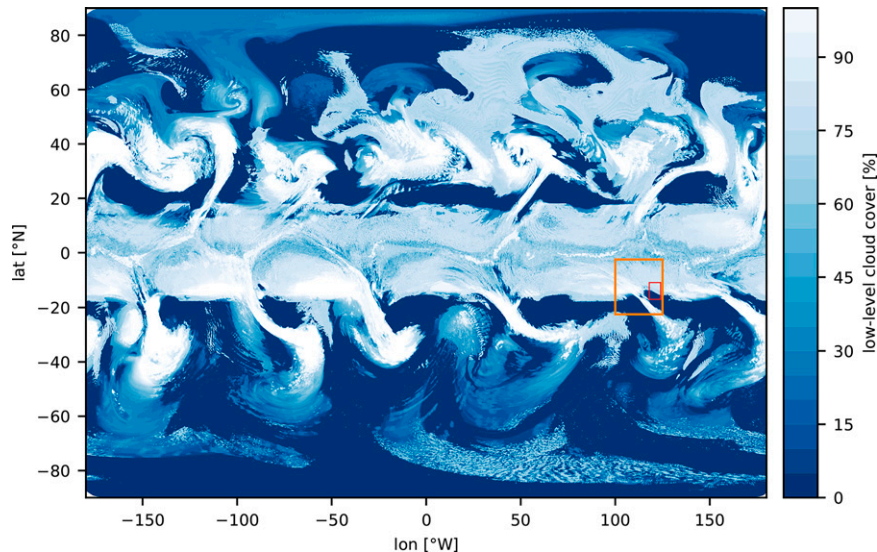
Fig. A4. Low-level cloud cover for a single time step from the global ICON-NWP simulation at Δ_h = 10 km. The orange rectangle indicates the LAM subdomain. The red rectangle indicates the LEM-6° subdomain.

yields 125 periods. For each period we calculate the time-mean domain mean of total, low-, mid-, and high-level cloud cover, column cloud ice and liquid, column water vapor, surface temperature, and SWCRE. We select a representative period, for which the time-mean domain-mean values are located within the inner quartiles of the distribution of the 125 periods (Fig. A1).

b. Selection of the LAM subdomain for NWP2.5

Analogously to choosing the 5-day period for NWP10, we choose a representative subdomain for NWP2.5 by analyzing 68 potential subdomains from NWP10. Each subdomain reaches from 2.5° to 22.5°S and spans 25° in longitudinal direction. The subdomains overlap by 5° longitude. Subdomains crossing 360° longitude are not considered. We choose a subdomain that is located at 100°–125° longitude (Fig. A2).

c. Selection of a 1-day period and the LEM-6° subdomain for LEM0.6

We choose a suitable subdomain and period for LEM0.6 by analyzing 80 spatial and temporal subsets of NWP2.5. We analyze 1-day periods starting each day, which yields four periods. For each period we analyze subdomains that span 6° longitude within the range 100°–125° longitude and overlap by 5° longitude. This yields 20 subdomains per period. The subdomains extend from 11° to 17° latitude.

Analogously to appendix section a, we calculate time and area means for each subset. Since we study shallow low-level clouds, we exclude subsets that exhibit mid- and high-level cloud cover exceeding 10%. By further selecting subsets for which surface temperature and column water vapor lie within the inner quartiles of the distributions, this leaves

us with two subsets. We choose the subset with stronger low-level cloud cover and stronger SWCRE (Fig. A3).

d. Overview over subdomains

Figure A4 shows the subdomains used for the LAM and LEM simulations superposed on a snapshot of low-level cloud cover as simulated by ICON-NWP.

REFERENCES

Abbot, D. S., and I. Halevy, 2010: Dust aerosol important for Snowball Earth deglaciation. *J. Climate*, **23**, 4121–4132, https://doi.org/10.1175/2010JCLI3378.1.

——, and R. T. Pierrehumbert, 2010: Mudball: Surface dust and Snowball Earth deglaciation. *J. Geophys. Res.*, **115**, D03104, https://doi.org/10.1029/2009JD012007.

——, A. Voigt, and D. Koll, 2011: The Jormungand global climate state and implications for Neoproterozoic glaciations. *J. Geophys. Res.*, **116**, D18103, https://doi.org/10.1029/2011JD015927.

——, ——, M. Branson, R. T. Pierrehumbert, D. Pollard, G. Le Hir, and D. D. B. Koll, 2012: Clouds and Snowball Earth deglaciation. *Geophys. Res. Lett.*, **39**, 2012GL052861, https://doi.org/10.1029/2012GL052861.

Bechtold, P., M. Koehler, T. Jung, F. Doblas-Reyes, M. Leutbecher, M. J. Rodwell, F. Vitart, and G. Balsamo, 2008: Advances in simulating atmospheric variability with the ECMWF model: From synoptic to decadal time-scales. *Quart. J. Roy. Meteor. Soc.*, **134**, 1337–1351, https://doi.org/10.1002/qj.289.

Boucher, O., and Coauthors, 2013: Clouds and aerosols. *Climate Change 2013: The Physical Science Basis*, T. F. Stocker et al., Eds., Cambridge University Press, 571–657.

Braun, C., J. Hörner, A. Voigt, and J. G. Pinto, 2022: Ice-free tropical waterbelt for Snowball Earth events questioned by

uncertain clouds. *Nat. Geosci.*, **15**, 489–493, https://doi.org/10.1038/s41561-022-00950-1.

Collins, W. D., and Coauthors, 2004: Description of the NCAR Community Atmosphere Model (CAM 3.0). NCAR Tech. Note NCAR/TN-464+STR, 214 pp., https://doi.org/10.5065/D63N21CH.

de Rooy, W. C., and Coauthors, 2013: Entrainment and detrainment in cumulus convection: An overview. *Quart. J. Roy. Meteor. Soc.*, **139** (670), 1–19, https://doi.org/10.1002/qj.1959.

Dipankar, A., B. Stevens, R. Heinze, C. Moseley, G. Zängl, M. Giorgetta, and S. Brdar, 2015: Large eddy simulation using the general circulation model ICON. *J. Adv. Model. Earth Syst.*, **7**, 963–986, https://doi.org/10.1002/2015MS000431.

Drugé, T., P. Nabat, M. Mallet, and S. Somot, 2021: Future evolution of aerosols and implications for climate change in the Euro-Mediterranean region using the CNRM-ALADIN63 regional climate model. *Atmos. Chem. Phys.*, **21**, 7639–7669, https://doi.org/10.5194/acp-21-7639-2021.

Feulner, G., C. Hallmann, and H. Kienert, 2015: Snowball cooling after algal rise. *Nat. Geosci.*, **8**, 659–662, https://doi.org/10.1038/ngeo2523.

Field, P. R., and Coauthors, 2017: Secondary ice production: Current state of the science and recommendations for the future. *Ice Formation and Evolution in Clouds and Precipitation: Measurement and Modeling Challenges, Meteor. Monogr.*, Vol. 58, Amer. Meteor. Soc., https://doi.org/10.1175/AMSMONOGRAPHS-D-16-0014.1.

Giorgetta, M. A., and Coauthors, 2018: ICON-A, the atmosphere component of the ICON Earth system model: I. Model description. *J. Adv. Model. Earth Syst.*, **10**, 1613–1637, https://doi.org/10.1029/2017MS001242.

Giorgi, F., 2019: Thirty years of regional climate modeling: Where are we and where are we going next? *J. Geophys. Res. Atmos.*, **124**, 5696–5723, https://doi.org/10.1029/2018JD030094.

Hande, L., C. Engler, C. Hoose, and I. Tegen, 2015: Seasonal variability of Saharan desert dust and ice nucleating particles over Europe. *Atmos. Chem. Phys.*, **15**, 4389–4397, https://doi.org/10.5194/acp-15-4389-2015.

Heinze, R., and Coauthors, 2017: Large-eddy simulations over Germany using ICON: A comprehensive evaluation. *Quart. J. Roy. Meteor. Soc.*, **143**, 69–100, https://doi.org/10.1002/qj.2947.

Hoffman, P. F., 2016: Cryoconite pans on Snowball Earth: Supraglacial oases for Cryogenian eukaryotes? *Geobiology*, **14**, 531–542, https://doi.org/10.1111/gbi.12191.

——, A. J. Kaufman, G. P. Halverson, and D. P. Schrag, 1998: A Neoproterozoic Snowball Earth. *Science*, **281**, 1342–1346, https://doi.org/10.1126/science.281.5381.1342.

——, and Coauthors, 2017: Snowball Earth climate dynamics and Cryogenian geology-geobiology. *Sci. Adv.*, **3**, e1600983, https://doi.org/10.1126/sciadv.1600983.

Hohenegger, C., L. Kornblueh, D. Klocke, T. Becker, G. Cioni, J. F. Engels, U. Schulzweida, and B. Stevens, 2020: Climate statistics in global simulations of the atmosphere, from 80 to 2.5 km grid spacing. *J. Meteor. Soc. Japan*, **98**, 2020–005, https://doi.org/10.2151/jmsj.2020-005.

Hoose, C., and O. Möhler, 2012: Heterogeneous ice nucleation on atmospheric aerosols: A review of results from laboratory experiments. *Atmos. Chem. Phys.*, **12**, 9817–9854, https://doi.org/10.5194/acp-12-9817-2012.

Hourdin, F., and Coauthors, 2017: The art and science of climate model tuning. *Bull. Amer. Meteor. Soc.*, **98**, 589–602, https://doi.org/10.1175/BAMS-D-15-00135.1.

Hyde, W. T., T. J. Crowley, S. K. Baum, and W. R. Peltier, 2000: Neoproterozoic 'snowball Earth' simulations with a coupled climate/ice-sheet model. *Nature*, **405**, 425–429, https://doi.org/10.1038/35013005.

Kageyama, M., and Coauthors, 2017: The PMIP4 contribution to CMIP6–Part 4: Scientific objectives and experimental design of the PMIP4-CMIP6 Last Glacial Maximum experiments and PMIP4 sensitivity experiments. *Geosci. Model Dev.*, **10**, 4035–4055, https://doi.org/10.5194/gmd-10-4035-2017.

Kanji, Z. A., L. A. Ladino, H. Wex, Y. Boose, M. Burkert-Kohn, D. J. Cziczo, and M. Krämer, 2017: Overview of ice nucleating particles. *Ice Formation and Evolution in Clouds and Precipitation: Measurement and Modeling Challenges, Meteor. Monogr.*, No. 58, Amer. Meteor. Soc., https://doi.org/10.1175/AMSMONOGRAPHS-D-16-0006.1.

Kirschvink, J. L., 1992: Late Proterozoic low-latitude global glaciation: The snowball Earth. *The Proterozoic Biosphere: A Multidisciplinary Study*, J. W. Schopf, C. Klein, and D. Des Maris, Eds., Cambridge University Press, 51–52.

Klein, S. A., A. Hall, J. R. Norris, and R. Pincus, 2017: Low-cloud feedbacks from cloud-controlling factors: A review. *Surv. Geophys.*, **38**, 1307–1329, https://doi.org/10.1007/s10712-017-9433-3.

Korolev, A., and Coauthors, 2017: Mixed-phase clouds: Progress and challenges. *Ice Formation and Evolution in Clouds and Precipitation: Measurement and Modeling Challenges, Meteor. Monogr.*, No. 58, https://doi.org/10.1175/AMSMONOGRAPHS-D-17-0001.1.

Lebo, Z., and H. Morrison, 2015: Effects of horizontal and vertical grid spacing on mixing in simulated squall lines and implications for convective strength and structure. *Mon. Wea. Rev.*, **143**, 4355–4375, https://doi.org/10.1175/MWR-D-15-0154.1.

Lee, L., K. Pringle, C. Reddington, G. Mann, P. Stier, D. Spracklen, J. Pierce, and K. Carslaw, 2013: The magnitude and causes of uncertainty in global model simulations of cloud condensation nuclei. *Atmos. Chem. Phys.*, **13**, 8879–8914, https://doi.org/10.5194/acp-13-8879-2013.

Le Hir, G., Y. Donnadieu, G. Krinner, and G. Ramstein, 2010: Toward the Snowball Earth deglaciation. *Climate Dyn.*, **35**, 285–297, https://doi.org/10.1007/s00382-010-0748-8.

Li, D., and R. T. Pierrehumbert, 2011: Sea glacier flow and dust transport on Snowball Earth. *Geophys. Res. Lett.*, **38**, L17501, https://doi.org/10.1029/2011GL048991.

Liu, P., Y. Liu, Y. Peng, J.-F. Lamarque, M. Wang, and Y. Hu, 2020: Large influence of dust on the Precambrian climate. *Nat. Commun.*, **11**, 4427, https://doi.org/10.1038/s41467-020-18258-2.

Liu, Y., P. Liu, D. Li, Y. Peng, and Y. Hu, 2021: Influence of dust on the initiation of Neoproterozoic snowball Earth events. *J. Climate*, **34**, 6673–6689, https://doi.org/10.1175/JCLI-D-20-0803.1.

Love, G. D., and Coauthors, 2009: Fossil steroids record the appearance of Demospongiae during the Cryogenian period. *Nature*, **457**, 718–721, https://doi.org/10.1038/nature07673.

Macdonald, F. A., and R. Wordsworth, 2017: Initiation of Snowball Earth with volcanic sulfur aerosol emissions. *Geophys. Res. Lett.*, **44**, 1938–1946, https://doi.org/10.1002/2016GL072335.

Madonna, E., H. Wernli, H. Joos, and O. Martius, 2014: Warm conveyor belts in the ERA-Interim dataset (1979–2010). Part I: Climatology and potential vorticity evolution. *J. Climate*, **27**, 3–26, https://doi.org/10.1175/JCLI-D-12-00720.1.

McCoy, D. T., D. L. Hartmann, M. D. Zelinka, P. Ceppi, and D. P. Grosvenor, 2015: Mixed-phase cloud physics and Southern

Ocean cloud feedback in climate models. *J. Geophys. Res. Atmos.*, **120**, 9539–9554, https://doi.org/10.1002/2015JD023603.

McGraw, Z., T. Storelvmo, R. O. David, and N. Sagoo, 2020: Global radiative impacts of mineral dust perturbations through stratiform clouds. *J. Geophys. Res. Atmos.*, **125**, https://doi.org/10.1029/2019JD031807.

Mironov, D., B. Ritter, J.-P. Schulz, M. Buchhold, M. Lange, and E. MacHulskaya, 2012: Parameterisation of sea and lake ice in numerical weather prediction models of the German Weather Service. *Tellus*, **64A**, 17330, https://doi.org/10.3402/tellusa.v64i0.17330.

Mlawer, E. J., S. J. Taubman, P. D. Brown, M. J. Iacono, and S. A. Clough, 1997: Radiative transfer for inhomogeneous atmospheres: RRTM, a validated correlated-*k* model for the longwave. *J. Geophys. Res.*, **102**, 16663–16682, https://doi.org/10.1029/97JD00237.

Morris, J. L., and Coauthors, 2018: The timescale of early land plant evolution. *Proc. Natl. Acad. Sci. USA*, **115**, E2274–E2283, https://doi.org/10.1073/pnas.1719588115.

Phillips, V. T., P. J. DeMott, and C. Andronache, 2008: An empirical parameterization of heterogeneous ice nucleation for multiple chemical species of aerosol. *J. Atmos. Sci.*, **65**, 2757–2783, https://doi.org/10.1175/2007JAS2546.1.

Pierrehumbert, R., D. Abbot, A. Voigt, and D. Koll, 2011: Climate of the Neoproterozoic. *Annu. Rev. Earth Planet. Sci.*, **39**, 417–460, https://doi.org/10.1146/annurev-earth-040809-152447.

Prill, F., D. Reinert, D. Rieger, and G. Zängl, 2020: Working with the ICON Model: Practical exercises for NWP mode and ICON-ART. *Deutscher Wetterdienst Tech. Rep.*, https://code.mpimet.mpg.de/attachments/download/19568/ICON_tutorial_2019.pdf.

Raschendorfer, M., 2001: The new turbulence parameterization of LM. *COSMO Newsletter*, No. 1, Consortium for Small-Scale Modelling, Offenbach, Germany, 89–97, http://www.cosmo-model.org/content/model/documentation/newsLetters/newsLetter01/newsLetter_01.pdf.

Rauterkus, R., and C. Ansorge, 2020: Cloud-top entrainment in mixed-phase stratocumulus and its process-level representation in large-eddy simulation. *J. Atmos. Sci.*, **77**, 4109–4127, https://doi.org/10.1175/JAS-D-19-0221.1.

Rodehacke, C. B., A. Voigt, F. Ziemen, and D. S. Abbot, 2013: An open ocean region in Neoproterozoic glaciations would have to be narrow to allow equatorial ice sheets. *Geophys. Res. Lett.*, **40**, 5503–5507, https://doi.org/10.1002/2013GL057582.

Rose, B. E. J., 2015: Stable "Waterbelt" climates controlled by tropical ocean heat transport: A nonlinear coupled climate mechanism of relevance to Snowball Earth. *J. Geophys. Res. Atmos.*, **120**, 1404–1423, https://doi.org/10.1002/2014JD022659.

Sagoo, N., and T. Storelvmo, 2017: Testing the sensitivity of past climates to the indirect effects of dust. *Geophys. Res. Lett.*, **44**, 5807–5817, https://doi.org/10.1002/2017GL072584.

Sakradzija, M., A. Seifert, and A. Dipankar, 2016: A stochastic scale-aware parameterization of shallow cumulus convection across the convective gray zone. *J. Adv. Model. Earth Syst.*, **8**, 786–812, https://doi.org/10.1002/2016MS000634.

Segal, Y., and A. Khain, 2006: Dependence of droplet concentration on aerosol conditions in different cloud types: Application to droplet concentration parameterization of aerosol conditions. *J. Geophys. Res.*, **111**, D15204, https://doi.org/10.1029/2005JD006561.

Seifert, A., and K. D. Beheng, 2006: A two-moment cloud microphysics parameterization for mixed-phase clouds. Part 1: Model description. *Meteor. Atmos. Phys.*, **92**, 45–66, https://doi.org/10.1007/s00703-005-0112-4.

——, C. Köhler, and K. Beheng, 2011: Aerosol-cloud-precipitation effects over Germany as simulated by a convective-scale numerical weather prediction model. *Atmos. Chem. Phys.*, **11**, 203–220, https://doi.org/10.5194/acpd-11-20203-2011.

Senf, F., A. Voigt, N. Clerbaux, A. Hünerbein, and H. Deneke, 2020: Increasing resolution and resolving convection improve the simulation of cloud-radiative effects over the North Atlantic. *J. Geophys. Res. Atmos.*, **125**, e2020JD032667, https://doi.org/10.1029/2020JD032667.

Sherwood, S. C., S. Bony, and J.-L. Dufresne, 2014: Spread in model climate sensitivity traced to atmospheric convective mixing. *Nature*, **505**, 37–42, https://doi.org/10.1038/nature12829.

Sledd, A., and T. L'Ecuyer, 2019: How much do clouds mask the impacts of Arctic sea ice and snow cover variations? Different perspectives from observations and reanalyses. *Atmosphere*, **10**, 12, https://doi.org/10.3390/atmos10010012.

Smagorinsky, J., 1963: General circulation experiments with the primitive equations: I. The basic experiment. *Mon. Wea. Rev.*, **91**, 99–164, https://doi.org/10.1175/1520-0493(1963)091<0099:GCEWTP>2.3.CO;2.

Stevens, B., and Coauthors, 2020: The added value of large-eddy and storm-resolving models for simulating clouds and precipitation. *J. Meteor. Soc. Japan*, **98**, 395–435, https://doi.org/10.2151/jmsj.2020-021.

Stevens, D. E., A. S. Ackerman, and C. S. Bretherton, 2002: Effects of domain size and numerical resolution on the simulation of shallow cumulus convection. *J. Atmos. Sci.*, **59**, 3285–3301, https://doi.org/10.1175/1520-0469(2002)059<3285:EODSAN>2.0.CO;2.

Storelvmo, T., and I. Tan, 2015: The Wegener–Bergeron–Findeisen process—Its discovery and vital importance for weather and climate. *Meteor. Z.*, **24**, 455–461, https://doi.org/10.1127/metz/2015/0626.

Tiedtke, M., 1989: A comprehensive mass flux scheme for cumulus parameterization in large-scale models. *Mon. Wea. Rev.*, **117**, 1779–1800, https://doi.org/10.1175/1520-0493(1989)117<1779:ACMFSF>2.0.CO;2.

Twomey, S., 1977: The influence of pollution on the shortwave albedo of clouds. *J. Atmos. Sci.*, **34**, 1149–1152, https://doi.org/10.1175/1520-0469(1977)034<1149:TIOPOT>2.0.CO;2.

Vergara-Temprado, J., and Coauthors, 2018: Strong control of Southern Ocean cloud reflectivity by ice-nucleating particles. *Proc. Natl. Acad. Sci. USA*, **115**, 2687–2692, https://doi.org/10.1073/pnas.1721627115.

Walsh, A., T. Ball, and D. M. Schultz, 2019: Extreme sensitivity in Snowball Earth formation to mountains on PaleoProterozoic supercontinents. *Sci. Rep.*, **9**, 2349, https://doi.org/10.1038/s41598-019-38839-6.

Weisman, M. L., W. C. Skamarock, and J. B. Klemp, 1997: The resolution dependence of explicitly modeled convective systems. *Mon. Wea. Rev.*, **125**, 527–548, https://doi.org/10.1175/1520-0493(1997)125<0527: TRDOEM>2.0.CO;2.

Wilson, T. W., and Coauthors, 2015: A marine biogenic source of atmospheric ice-nucleating particles. *Nature*, **525**, 234–238, https://doi.org/10.1038/nature14986.

Wood, R., and C. S. Bretherton, 2006: On the relationship between stratiform low cloud cover and lower-tropospheric

stability. *J. Climate*, **19**, 6425–6432, https://doi.org/10.1175/JCLI3988.1.

Wu, J., Y. Liu, and Z. Zhao, 2021: How should snowball Earth deglaciation start. *J. Geophys. Res. Atmos.*, **126**, e2020JD033833, https://doi.org/10.1029/2020JD033833.

Zängl, G., D. Reinert, P. Rípodas, and M. Baldauf, 2015: The ICON (ICOsahedral Non-hydrostatic) modelling framework of DWD and MPI-M: Description of the non-hydrostatic dynamical core. *Quart. J.. Roy. Meteor. Soc.*, **141**, 563–579, https://doi.org/10.1002/qj. 2378.